

# A new measurement of the Hubble constant using Type Ia supernovae calibrated with surface brightness fluctuations

Nandita Khetan<sup>1,2</sup>, Luca Izzo<sup>3</sup>, Marica Branchesi<sup>1,2,4</sup>, Radosław Wojtak<sup>3</sup>, Michele Cantiello<sup>4</sup>, Chandrashekhar Murugesan<sup>5</sup>, Adriano Agnello<sup>3</sup>, Enrico Cappellaro<sup>6</sup>, Massimo Della Valle<sup>7</sup>, Christa Gall<sup>3</sup>, Jens Hjorth<sup>3</sup>, Stefano Benetti<sup>6</sup>, Enzo Brocato<sup>4,8</sup>, Jamison Burke<sup>9,10</sup>, Daichi Hiramatsu<sup>9,10</sup>, D. Andrew Howell<sup>9,10</sup>, Lina Tomasella<sup>6</sup>, Stefano Valenti<sup>11</sup>

<sup>1</sup> Gran Sasso Science Institute, Viale F. Crispi 7, I-67100 LAquila (AQ), Italy

<sup>2</sup> INFN, Laboratori Nazionali del Gran Sasso, I-67100 Assergi, Italy

<sup>3</sup> DARK, Niels Bohr Institute, University of Copenhagen, Jagtvej 128, 2200 Copenhagen, Denmark

<sup>4</sup> INAF, Osservatorio Astronomico d'Abruzzo, Via Mentore Maggini, Teramo, I-64100, Italy

<sup>5</sup> Centre for Astrophysics and Supercomputing, Swinburne University of Technology, Hawthorn, Victoria 3122, Australia

<sup>6</sup> INAF, Osservatorio Astronomico di Padova, Vicoletto dell'Osservatorio 5, 35122- Padova, Italy

<sup>7</sup> INAF, Osservatorio Astronomico di Capodimonte, Salita Moiariello 16, 80131- Naples, Italy

<sup>8</sup> INAF, Osservatorio Astronomico di Roma, Via Frascati 33, 00040, Monte Porzio Catone (RM), Italy

<sup>9</sup> Las Cumbres Observatory, Goleta, California 93117, USA

<sup>10</sup> Department of Physics, University of California, Santa Barbara, California 93106, USA

<sup>11</sup> Department of Physics, University of California, 1 Shields Avenue, Davis, CA 95616-5270, USA

e-mail: nandita.khetan@gssi.it

June 20, 2022

## ABSTRACT

We present a new calibration of the peak absolute magnitude of SNe Type Ia based on the Surface Brightness Fluctuations (SBF) method, aimed at measuring the value of the Hubble constant. We build a sample of calibrating anchors consisting of 24 SNe hosted in galaxies having SBF distance measurements. Applying a hierarchical Bayesian approach, we calibrate the SNe luminosity and extend it into the Hubble flow by using a sample of 96 SNe Ia in the redshift range  $0.02 < z < 0.075$ , extracted from the Combined Pantheon Sample. We estimate a value of  $H_0 = 70.50 \pm 2.37(\text{stat}) \pm 3.38(\text{sys}) \text{ km s}^{-1} \text{ Mpc}^{-1}$  (i.e. 3.4% stat, 4.8% sys), which is in agreement with the value obtained using the tip of the red giant branch calibration, and consistent within the errors with the value obtained from SNe Type Ia calibrated with Cepheids and the one inferred from the analysis of the cosmic microwave background. We find that the SNe Ia distance moduli calibrated with SBF are on average larger by 0.07 mag than the ones calibrated with Cepheids. Our results point to possible differences among SNe in different types of galaxies, which could originate from different local environments and/or SNe Ia progenitor properties. Sampling different host galaxy type, SBF offers a complementary approach to Cepheids which is important in addressing possible systematics. As the SBF method has the ability to reach larger distances than Cepheids, the impending entry of LSST and JWST into operation will increase the number of SNe Ia hosted in galaxies where SBF distances can be measured, making SBF measurements attractive for improving the calibration of SNe Ia, and in the estimation of  $H_0$ .

**Key words.** supernovae: general, Cosmology: distance scale, Cosmology: observations

## 1. Introduction

The standard cosmological model, also known as  $\Lambda$  cold dark matter ( $\Lambda$ CDM) scenario, represents the only model which is consistent with a wide set of observations from different epochs of the Universe. This concordance model describes our universe as flat, accelerating and primarily being composed of baryons, dark matter and dark energy, with the latter two components being the most dominant constituents at the present time, although the most elusive ones. One of the fundamental parameters governing the  $\Lambda$ CDM model is the Hubble constant ( $H_0$ ), which sets the absolute scale of the universe and can be measured both at early epochs, by the size of the sound horizon from the cosmic microwave background (CMB, [Planck Collaboration et al. 2016](#); [Bennett et al. 2013](#)), as well as in the local present-time universe using luminosity distance indicators ([Freedman et al. 2001](#); [Sandage et al. 2006](#); [Riess et al. 2016](#)). Comparing the absolute

scale at the two opposite ends of the expanding Universe sets a stringent test for the standard cosmological paradigm.

With extensive ongoing efforts,  $H_0$  measurements are achieving remarkable accuracy and precision at both these extremes. In the local universe regime, one of the most reliable measurements of  $H_0$  comes from SNe Ia, which however rely on primary distance indicators for their zero-point calibration (e.g. Cepheids and geometrical distances). The last couple of decades have witnessed gradual improvements in  $H_0$  measurements using SNe Ia (e.g. [Freedman et al. 2009, 2012](#); [Riess et al. 2011, 2016](#); [Dhawan et al. 2018](#); [Phillips et al. 2019](#)), with the most recent estimate by [Riess et al. \(2019\)](#) who obtain  $H_0 = 74.03 \pm 1.42 \text{ km s}^{-1} \text{ Mpc}^{-1}$  using the Cepheid calibration of the SNe Ia (*SHOES* program). Other powerful astrophysical probes measuring  $H_0$  include time-delay gravitational lensing (e.g. [Suyu et al. 2017](#); [Birrer et al. 2019](#)), the Tully-Fisher relation (e.g. [Sorce et al. 2013](#)), the Surface Brightness Fluctuations (e.g. [Jensen et al. 2001](#); [Cantiello et al. 2018b](#))

and the distance measurement using gravitational wave signals from binary compact objects (Abbott et al. 2017), to name a few.

In the early Universe, the latest estimate of the Hubble constant coming from the CMB observations by the Planck satellite is  $H_0 = 67.4 \pm 0.5 \text{ km s}^{-1} \text{ Mpc}^{-1}$  (Planck Collaboration et al. 2018). Another way of estimating  $H_0$  is through measurements of fluctuations in the matter density called as baryon acoustic oscillations (BAO, Cole et al. 2005; Eisenstein et al. 2005; Aubourg et al. 2015; Alam et al. 2017). The absolute calibration of BAO is based on prior knowledge of the sound horizon size, which depends on the early-time physics making it dependent on the CMB. Macaulay et al. (2019) measured a value  $H_0 = 67.77 \pm 1.30 \text{ km s}^{-1} \text{ Mpc}^{-1}$  using BAO and SNe Ia from the Dark Energy Survey (DES) where the absolute distance measurements from the BAOs were used to calibrate the intrinsic magnitude of the SNe Ia. This "inverse" distance ladder approach where the distance calibration is done through CMB or other high-redshift observations is not a direct method, it requires a cosmological model to build on.

The majority of the local independent methods or their combinations used to estimate  $H_0$  stand in sheer tension with the  $H_0$  values inferred from the CMB analysis, with discrepancies ranging between  $4\sigma$  and  $6\sigma$  (Verde et al. 2019). However, a recent calibration of SNe Ia using the tip of the red giant branch (TRGB) method in the color-magnitude diagram of SNe Ia host galaxies provided  $H_0 = 69.8 \pm 0.8(\pm 1.1\%\text{stat}) \pm 1.7(\pm 2.4\%\text{sys}) \text{ km s}^{-1} \text{ Mpc}^{-1}$  (Freedman et al. 2019). Using a different calibration of the TRGB in the Large Magellanic Cloud (LMC), Yuan et al. (2019) estimated  $H_0 = 72.4 \pm 2.0 \text{ km s}^{-1} \text{ Mpc}^{-1}$ . After a re-analysis of the LMC TRGB extinction, Freedman et al. (2020) confirmed their earlier estimate of  $H_0 = 69.6 \pm 0.8(\pm 1.1\%\text{stat}) \pm 1.7(\pm 2.4\%\text{sys}) \text{ km s}^{-1} \text{ Mpc}^{-1}$ , which sits between the Planck-CMB value and the one resulting from SNe Ia calibrated using Cepheids.

If the difference among local  $H_0$  measurements and the Planck-CMB one is statistically confirmed by future independent observations and analyses, it would hint at a possible flaw in the standard  $\Lambda$ CDM model and it would then imply the existence of some "new physics" beyond it, which includes new species of relativistic particles, non-zero curvature, dark radiation or even modification of the equations of general relativity (e.g. Bernal et al. 2016; Mörtzell & Dhawan 2018; Verde et al. 2019; Arendse et al. 2019). However, the proposed modifications of  $\Lambda$ CDM model appear in conflict with other existing cosmological tests and worsen the model fit to the observed CMB spectra. Neither new physics nor identifiable systematics are currently able to resolve the tension. In this scenario, new and independent  $H_0$  estimates and credible quantification of the systematic uncertainties (instrumental and astrophysical) are necessary.

Among all the Hubble flow distance indicators, SNe Ia are one of the most reliable probe for the  $H_0$  measurement. In the cosmic distance ladder approach, SNe Ia distances generally rely on some primary distance measurements in the nearby universe, like Cepheids (Riess et al. 2019) or the previously mentioned TRGB. The ladder approach to estimate  $H_0$  consists of three main steps: (1) absolute calibration of the primary distance indicator with geometric anchors, for example using parallaxes for Milky Way Cepheids (Gaia Collaboration et al. 2018) and/or for LMC Cepheids, detached eclipsing binaries (DEBs) (Pietrzyński et al. 2019), and masers (Riess et al. 2016); (2) Calibrating the luminosity of nearby SNe Ia using the distance from the primary indicator to SNe Ia host galaxies, and (3) using the calibrated relation between SNe Ia light curve properties and luminosity to measure distances to SNe Ia in the Hubble flow. Therefore, in

order to obtain precise distances and  $H_0$  estimates, it is necessary to control the various systematic errors entering in each of the above steps, to gather a statistically significant sample of galaxies hosting SNe Ia in the local universe to be used as calibrators, and to have accurate distance estimates to the galaxies of this calibrating sample via primary distance methods.

Presently, the *yardstick* measurement, which highlights the Hubble tension finding a higher  $H_0$  with respect to early-universe estimates is based on the calibration using Cepheid distance scale, in particular with Weisenheit magnitudes (Madore & Freedman 1991). This calibration currently relies on a sample of 19 nearby galaxies hosting SNe Ia and having their distances measured with Cepheids (*SHOES* sample, Supernovae  $H_0$  for the Equation of State of Dark energy, Riess et al. 2005, Riess et al. 2019). On the other hand, the  $H_0$  estimate based on a sample of 18 SNe Ia host galaxies having their distances measured with TRGB shows a lower value of the Hubble constant, which is in agreement at the  $1.2\sigma$  level with the Planck estimate (Freedman et al. 2020). In the wake of these results, it is imperative to exploit different methods to estimate precise distances in the local universe in order to confirm or resolve the Hubble tension.

In this context, this work aims at exploring the use of Surface Brightness Fluctuations (SBF) distance method to be employed as an anchor for measuring the distances to SNe Ia host galaxies into the Hubble flow. Ajhar et al. (2001) compared the SBF distances of galaxies hosting a SNe Ia with SNe Ia distance calibrated with Cepheids, and homogenised the SBF and SNe Ia distance scales. Based on this result, we propose for the first time to calibrate SNe Ia luminosity using SBF distances to their host galaxies, with the main goal of estimating the Hubble constant.

The possibility to measure accurate distances to early-type galaxies (and sometimes bulges of spiral galaxies) in the nearby universe with SBF was first introduced by Tonry & Schneider (1988). Detailed descriptions about the SBF methods are given in Blakeslee et al. (1999); Biscardi et al. (2008); Blakeslee et al. (2009a). The SBF method determines the intrinsic variance in a galaxy image resulting from stochastic variations in the numbers and luminosities of the stars falling within the individual pixels of the image. The measured variance is normalized by the local galaxy surface brightness and then converted to the apparent SBF magnitude  $\bar{m}$ . The distance modulus,  $\mu = \bar{m} - \bar{M}$ , is then obtained knowing the absolute SBF magnitude  $\bar{M}$ , which depends on the stellar population properties (Blakeslee et al. 2001; Mei et al. 2005; Cantiello et al. 2018a). The  $\bar{M}$  zero-point is tied directly to the Cepheid distance scale (empirical calibration, e.g. Tonry et al. 2001) or derived from stellar population models (theoretical calibration, e.g. Brocato et al. 1998; Cantiello et al. 2003; Raimondo et al. 2005; Marin-Franch & Aparicio 2006; Biscardi et al. 2008). The stellar populations dominated by evolved stars (with the red giant branch mostly contributing to the flux variance) in early-type galaxies, makes them the ideal galaxies to measure the distance through SBF measurements (Blakeslee 2012). The SBF technique enables us to measure distances with a precision of  $5 - 10\%$  up to  $\sim 100 \text{ Mpc}$  with the current instruments like the Hubble Space Telescope (Jensen et al. 2015).

Although the SBF distances are calibrated themselves using Cepheids, and represent a secondary calibrator method for SNe Ia, they offer potential advantages and useful insights in terms of identifying possible systematic effects associated with the luminosity calibration. While SNe calibrated with Cepheids, such as the ones in the *SHOES* sample are all hosted in late-type galaxies, the SBF distance measurements are available mainly for early-type host galaxies, making SBF calibrator sample complementary,

in terms of SN hosts, to the Cepheid sample. The comparison among the SBF and Cepheid calibrations enables us to identify possible systematics for SNe luminosities in different host galaxy types, as it was recently suggested (Kang et al. 2019).

Furthermore, early-type galaxies have generally less amount of dust when compared with late-type galaxies, and hence the host extinction, which remains a tricky issue for the SN light curve analysis (Tripp 1998; Burns et al. 2014; Brout & Scolnic 2020), is reduced. The distance range covered by SBF measurements significantly exceeds the one covered by the TRGB and Cepheid measurements and that helps to augment the number of calibrators. In terms of observational advantages, SBF can be performed on images which do not require the high resolution and depth necessary to resolve stellar photometry as for TRGB and Cepheids. Further, this method does not require periodic observations of the galaxies.

The paper is organized as follows. In Section 2, we describe the nearby SNe Ia samples used as calibrators and the distant cosmological sample used for  $H_0$  measurement. In Section 3, we explain the details of our analysis, and in Section 4, we give the Hubble diagram and our estimates of the Hubble constant. In Section 5, we evaluate the influence of the host galaxy type on the SNe Ia standardization by applying a galaxy stellar-mass correction. Section 6 compares the distance measurements obtained by applying the SBF and Cepheid calibrations. We discuss our results in Section 7, and we draw our conclusions and future prospects in Section 8.

## 2. Data

The choice and number of calibrators are key factors in defining the zero-point of the calibrating relation and eventually the accuracy of Hubble flow distance estimates, given that they determine the uncertainty on the  $H_0$  value. In order to appropriately calibrate the peak luminosity of SNe Ia with SBF distance indicators, we first identify all the galaxies hosting a SNe Ia and having a distance measurement evaluated through the SBF technique. Then, we filter this sample according to specific SNe Ia data quality criteria, which are reported below.

### 2.1. SBF Calibration sample

In order to build the SBF calibration sample, we cross-match the major published SBF distance catalogs (Tonry et al. 2001; Ajhar et al. 2001; Jensen et al. 2003; Mei et al. 2003; Cantiello et al. 2007; Blakeslee et al. 2009b; Cantiello et al. 2013, 2018a) with the SNe Ia catalog from Guillochon et al. (2017) available on the Open Supernova Catalog webpage<sup>1</sup>. The preliminary cross-matched sample consists of 45 galaxies. For the galaxies in this preliminary sample having multiple SBF distance estimates, we select the most recent estimate favoring the use of the Hubble Space Telescope (HST) data when available.

Taking into account the importance of the quality of the data of SNe light curves (LC) for a good calibration, we apply LC quality cuts in order to avoid any systematics caused by their irregularities. Our fiducial calibration sample consists of SNe Ia with: (1) high cadence observation data, especially around the maximum and within the first 40 days after the peak brightness, in order to accurately sample the LC evolution and constrain the peak magnitude; (2) regular light curve shape ( $s_{BV} > 0.5$  removing fast decliner cases, see Section 3 for the definition of the color-stretch parameter  $s_{BV}$ ); and (3) low reddening (color

$m_B - m_V < 0.3$  mag)<sup>2</sup>. Among the 45 SNe Ia in the preliminary sample, 24 pass the above quality cuts and form our final SBF calibrator sample.

For the photometry of the SNe in our calibrator sample, the optical ( $B$  and  $V$  band) light curves are taken from the published data assembled in Guillochon et al. (2017). The individual references for the photometric data of each object are given in Table A.1 of the Appendix A. Table 1 shows the SBF calibration sample listing the 24 SNe Ia selected to have high quality photometric data and standard light curve evolution. It lists the SNe Ia name (*column 1*), the host galaxy name (*column 2*), the SBF distance modulus along with the associated error (*columns 3 and 4*), the galaxy morphological type (*column 5*), the reference for the galaxy SBF distance (*column 6*) and the host galaxy stellar mass along with the error (*column 7 and 8*). The stellar mass for each SNe Ia host galaxy used in this work is computed using the Ks-band magnitude from the 2MASS survey (Skrutskie et al. 2006a) as described in the Appendix C.

All the SBF distances used in the present paper are tied to a common empirical zero-point based on the results of the *HST* Key Project (KP) Cepheid distances by Freedman et al. (2001) [hereafter, F01] as described in Blakeslee et al. (2002). The SBF zero-point calibration adopted by Tonry et al. (2001) was based on a previous estimate evaluated using six galaxies with KP Cepheid distances (Ferrarese et al. 2000) and needed a revision. A general correction formula for the published distances in Tonry et al. (2001) is provided by Blakeslee et al. (2010). This formula includes both the zero-point as well as second-order bias correction which takes into account the variation of the data quality. All the distances from Tonry et al. (2001) in this work are corrected according to this formula bringing them to the same zero-point of the other SBF measurements in the present sample. F01 adopt the Cepheid Period-Luminosity ( $P$ - $L$ ) relations by Udalski et al. (1999), and the metallicity corrections to the Cepheid distances by Kennicutt et al. (1998).

It is worth noting that our SBF distances are calibrated to the Cepheid zero-point based on Cepheid distances by F01, who adopted an LMC distance modulus of  $18.50 \pm 0.10$  mag. Riess et al. (2016) for the Cepheid distances of the SH0ES sample SNe (described in the next subsection) used a LMC distance of  $18.493 \pm 0.008(\text{stat}) \pm 0.047(\text{sys})$  mag based on 8 DEBs (Pietrzynski et al. 2013). The most recent value by Pietrzynski et al. (2019) which is anchored on 20 DEB stars in the LMC gives  $\mu_{LMC} = 18.477 \pm 0.004(\text{stat}) \pm 0.026(\text{sys})$  mag and has been adopted by Riess et al. (2019) for the Cepheid distances and by Freedman et al. (2019) for the TRGB estimates.

The statistical errors on SBF distances for all the objects are taken as reported in the corresponding papers. The systematic error has been estimated including the uncertainty in the tie of the SBF distances to the Cepheid distance scale, which is evaluated to be of 0.1 mag (see e.g. Freedman & Madore 2010; Cantiello et al. 2018b) and represents the largest contribution to the systematic error.

### 2.2. SH0ES calibration sample

In order to compare the SNe Ia distances and the  $H_0$  estimated using the SBF calibration with those estimated from Cepheid calibration, we also take the SH0ES sample of 19 galaxies from Riess et al. (2016, 2019) as second calibrator set. These galaxies hosting a SNe Ia have their distances estimated using Cepheid

<sup>2</sup>  $m_B - m_V$  throughout this work refers to the pseudocolor derived from the maximum brightness in the  $B$  and the  $V$  bands.

<sup>1</sup> <https://sne.space/>

**Table 1.** Calibrator sample of SNe Ia hosted in galaxies that have SBF distance modulus measurements. These 24 SNe Ia listed here in the table form the SBF calibrator sample used in this work.

Supernova	Host Galaxy	$\mu_{SBF}$ (mag)	$\sigma_{SBF}$ (mag)	Morpholgy	Distance Reference	$\log M_*$ ( $M_\odot$ )	$\sigma_{\log M_*}$ ( $M_\odot$ )
SN2000cx	NGC524	31.921	0.212	SA0(rs)	Tonry et al. (2001)	10.929	0.090
SN1994D	NGC4526	31.320	0.120	SAB0(s)	Cantiello et al. (2018a)	10.996	0.055
SN2007on	NGC1404	31.526	0.072	E1	Blakeslee et al. (2009a)	10.932	0.035
SN2012cg	NGC4424	31.020	0.180	SB(s)a	Cantiello et al. (2018a)	9.706	0.083
SN1980N	NGC1316	31.590	0.050	SAB0(s)pec	Cantiello et al. (2013)	11.514	0.032
SN2003hv	NGC1201	31.566	0.304	SA0(r)	Tonry et al. (2001)	10.565	0.064
SN2008Q	NGC524	31.921	0.212	SA0(rs)	Tonry et al. (2001)	10.929	0.090
SN1970J	NGC7619	33.582	0.151	E	Mei et al. (2003)	11.340	0.073
SN1983G	NGC4753	31.919	0.197	I0	Tonry et al. (2001)	11.148	0.064
SN2014bv	NGC4386	32.190	0.494	SAB0	Tonry et al. (2001)	10.480	0.064
SN2015bp	NGC5839	31.737	0.314	SAB0(rs)	Tonry et al. (2001)	9.979	0.137
SN2016coj	NGC4125	31.922	0.258	E6 pec	Tonry et al. (2001)	11.083	0.064
SN1981D	NGC1316	31.590	0.050	SAB0(s)pec	Cantiello et al. (2013)	11.514	0.032
SN1992A	NGC1380	31.632	0.075	SA0	Blakeslee et al. (2009a)	10.931	0.032
SN2018aoz	NGC3923	31.795	0.101	E4-5	Cantiello et al. (2007)	11.204	0.065
SN2011iv	NGC1404	31.526	0.072	E1	Blakeslee et al. (2009a)	10.932	0.035
SN2006dd	NGC1316	31.590	0.050	SAB(s)pec	Cantiello et al. (2013)	11.514	0.032
SN1992bo	E352-057	34.270	0.150	SB0(s)pec	Ajhar et al. (2001)	10.395	0.071
SN1997E	NGC2258	33.500	0.150	SA0(r)	Ajhar et al. (2001)	11.199	0.069
SN1995D	NGC2962	32.600	0.150	SAB0(rs)	Ajhar et al. (2001)	10.597	0.069
SN1996X	NGC5061	32.260	0.190	E0	Ajhar et al. (2001)	11.057	0.086
SN1998bp	NGC6495	33.100	0.150	E	Ajhar et al. (2001)	10.462	0.069
SN2017fgc	NGC474	32.536	0.133	SA0(s)	Cantiello et al. (2007)	10.568	0.061
SN2020ue	NGC4636	30.830	0.130	E0	Tonry et al. (2001)	10.803	0.061

variable stars. Their distance moduli (and associated uncertainties) are taken from Table 5 of [Riess et al. \(2016\)](#) [hereafter, [R16](#)], and the photometric data of the SNe Ia are retrieved from the Open Supernova Catalog.

The Cepheid distances taken from [R16](#) are calibrated using the near-infrared (NIR) and optical Cepheid  $P$ - $L$  relations. Using only the optical relation they find  $H_0 = 71.56 \pm 2.49$ , which is  $\sim 2\%$  smaller than the NIR-based estimate of  $H_0 = 73.24 \pm 1.74$ . The optical Cepheid  $P$ - $L$  relations used by [R16](#) are described in [Hoffmann et al. \(2016\)](#), where it is also shown that their optical  $P$ - $L$  relations are in very good agreement with the  $P$ - $L$  relations of [Udalski et al. \(1999\)](#), adopted in [F01](#). Moreover, three of the 19 *SHOES* calibrators are also present in [F01](#), namely NGC1365, NGC4536 and NGC4639. For these three galaxies, the difference between the distance modulus from [R16](#) and the metallicity corrected one from [F01](#) is 0.04, 0.04 and -0.18 mag, respectively. Although it is not a statistically significant comparison, they show no systematic offset.

Multiple SNe Ia analyses show correlations between luminosity of the SNe and the host galaxy mass (e.g. [Kelly et al. 2010](#); [Lampeitl et al. 2010](#); [Sullivan et al. 2010](#); [Gupta et al. 2011](#)), age, metallicity and star formation rate (SFR) (e.g. [Hayden et al. 2013](#); [Rigault et al. 2013, 2015](#); [Roman et al. 2018](#)). Thus, the SNe luminosity dependence on host galaxy properties is another important ingredient which should be taken into account for any SNe Ia studies. Differences between the properties of the host galaxies of the calibrating sample and that of the Hubble-flow sample may introduce systematic errors in the value of  $H_0$  (see

e.g. [Freedman et al. 2019](#)). Different host environments can also affect the extinction suffered by the SNe luminosity, which is another issue to be addressed in SNe Ia cosmology ([Brout & Scolnic 2020](#)).

The *SHOES* sample is mainly composed of late-type spiral galaxies as Cepheids are relatively young stars. On the other hand, the SBF sample is biased towards early galaxies (92% of the SBF sample) dominated by old stellar populations. Figure 1 shows the histograms (top panel) and the density distributions (bottom panel) of the stellar mass of the host galaxies belonging to the SBF and *SHOES* calibrator samples. The *SHOES* sample shows a lower mean galaxy stellar-mass (log stellar masses in units of  $M_\odot$ ) of 9.97 than the SBF sample (10.87). We note that only one SN, namely SN2012cg hosted in NGC4424, is common among the two calibrator samples. For comparison, the Figure 1 also shows the distribution of the host-galaxy stellar masses for the cosmological sample described in the next section.

### 2.3. Cosmological Sample

For measuring the Hubble constant, we build a statistically significant sample of SNe Ia extending into the Hubble flow. We extract our cosmological sample from the big Combined Pantheon Sample ([Scolnic et al. 2018](#)) which consists of 1048 spectroscopically confirmed SNe Ia coming from various local and high-redshift supernovae surveys. All the SNe are cross-calibrated with the Pan-STARRS (PS1) survey in order to have a common photometric calibration ([Scolnic et al. 2015](#)). We select all the SNe

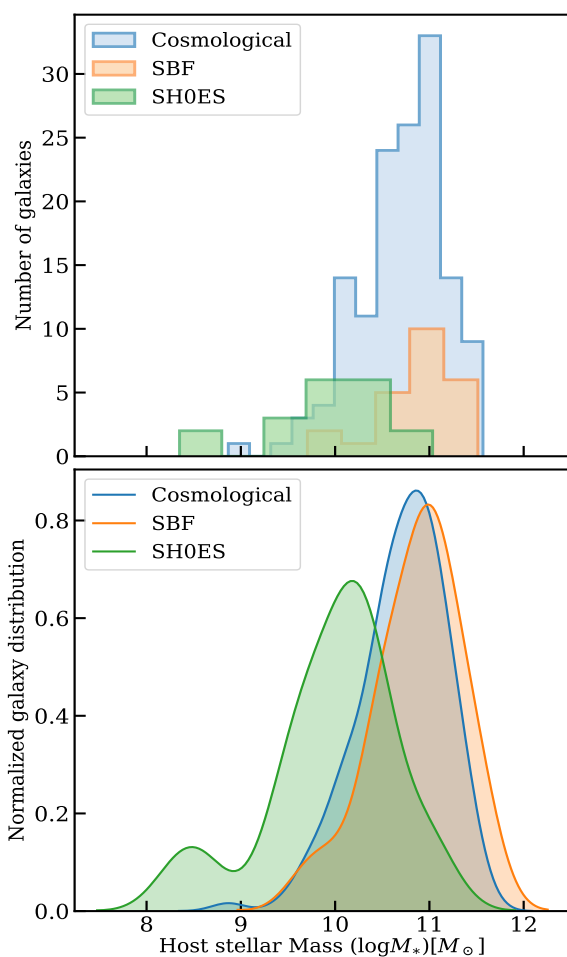


**Fig. 1.** The number of galaxies (top panel) and the normalized density distribution (bottom panel) as a function of the host galaxy stellar mass for the SBF and the *SH0ES* calibrator samples. We also plot the host stellar mass distribution for the cosmological sample. The KS-test P value for the two calibrator samples gives  $6.03 \times 10^{-6}$  indicating that the stellar mass distributions of the SNe Ia host galaxies are different for the two samples.

Ia spanning a redshift range of  $0.009 < z < 0.075$ , with good quality photometric data to appropriately sample the LC, and with 2MASS Ks-band magnitude to evaluate the galaxy stellar-mass. We also exclude fast decliners and very red SNe Ia from the sample (as described in Section 3). This gives us a sample of 140 SNe Ia, called full cosmological sample hereafter.

The main contributions to the data sample come from the Harvard Smithsonian Center for Astrophysics CfA1-CfA4 (Riess et al. 1999; Jha et al. 2006; Hicken et al. 2009a,b, 2012) and the Carnegie Supernova Project (CSP, Contreras et al. 2010; Folatelli et al. 2010; Stritzinger et al. 2011) survey. The optical photometric data of the cosmological sample SNe are assembled using data stored in a dedicated repository<sup>3</sup>, and are analyzed in the same way as the data of the SNe Ia belonging to the calibrator samples.

Since the lower redshift range of this cosmological sample starts with  $z = 0.009$  where peculiar velocities can have a significant impact on the recessional velocities of the galaxies, we apply a more stringent redshift cut removing all galaxies below  $z = 0.02$  (similar to R16) in order to mitigate the contamination

from peculiar velocities. This sample cut leaves 96 galaxies in the cosmological set and is referred to as the redshift-cut cosmological sample throughout this work. Our main results will be then based on the use of the redshift-cut cosmological sample, although we will also estimate  $H_0$  using the full cosmological sample for comparison with studies such as Freedman et al. (2019).

To summarize, this work has two calibrator sets: the SBF sample which is our main sample consisting of 24 SNe Ia, and the *SH0ES* sample from R16 having 19 SNe Ia. The calibrations derived from these two are applied to the full cosmological sample consisting of 140 SNe Ia and its sub-sample of 96 SNe Ia with the redshift cut.

### 3. Analysis

While the exact nature of SNe Ia progenitors remains uncertain, the regularity of their observed properties enables us to use them for measuring precise distances. This relies on the empirical evidence that their intrinsic luminosity is correlated with the rate of decline of their light curves and hence they can be standardized (Phillips 1993; Riess et al. 1996; Perlmutter et al. 1997). Considering this and further implementing correction terms which take into account the absolute luminosity dependence on the color and the host galaxy, SNe Ia can be used as standard candles for cosmological studies.

#### 3.1. Lightcurve fitting

In order to evaluate the SNe Ia luminosity from the observable LC properties, we fit the LCs of all the SNe Ia in this study belonging to the two calibrator samples and the cosmological sample. We estimate their apparent magnitudes at maximum in the B and V bands, along with the light curve shape. For this, we use the SNoPy (SuperNovae in Object Oriented Python) LC fitter (Burns et al. 2011). SNoPy corrects the photometry data for Milky Way extinction using the dust maps of Schlafly & Finkbeiner (2011), and applies the K-corrections that are computed using the SED template sequence developed by Hsiao et al. (2007). We fit the LC using the 'max-model' method<sup>4</sup> which gives us the epoch and the magnitude (for each filter) of the LC maximum, and the LC shape parameter  $s_{BV}$ , called the 'color-stretch' parameter (Burns et al. 2014).

The 'color-stretch' parameter takes into account the color ( $m_B - m_V$ ) evolution of the SNe Ia and is calculated by getting the time between B maximum and ( $m_B - m_V$ ) maximum (the typical value for which is 30 days) and dividing this time by 30. We use  $s_{BV}$  as the LC shape parameter, instead of the more commonly used  $\Delta m_{15}$  (magnitude decline between the LC maximum and 15 days later) because  $s_{BV}$  properly captures the behavior of fast decliners and it is appropriately sensitive to the extinction (Burns et al. 2014, 2018). For 'normal' SNe Ia  $s_{BV}$  is about 1, while for fast decliners  $s_{BV}$  is typically smaller than 0.5. We exclude from our fiducial calibrator sample fast decliner SNe Ia ( $s_{BV} < 0.5$ ) and highly reddened SNe Ia ( $m_B - m_V > 0.3$  mag). The calibrator sample contains two "transitional" objects, namely SN 2007on and SN 2011iv both located in NGC 1404, characterised by peak magnitudes similar to normal SNe Ia but with a relatively faster rate of decline (Gall et al. 2018). Since the use of the color-stretch parameterization in their LC fitting should ensure a reliable modelling for their evolution, we include

<sup>3</sup> <http://snana.uchicago.edu/downloads.php>

<sup>4</sup> For details see the online documentation of SNoPy: <https://csp.obs.carnegiescience.edu/data/snpy/documentation>

them in our fiducial calibrator sample maintaining the threshold  $s_{BV} > 0.5$  as done in previous works, such as Freedman et al. (2019) and Burns et al. (2018). However, we also perform the analysis excluding them from the sample to investigate their influence on the final results (see Section 4).

Table 2 lists the LC parameters for the SBF calibrator sample; the maximum magnitude in B and V band along with the errors (Columns 2-5), the  $s_{BV}$  parameter and relative error (Columns 6 and 7), the color ( $m_B - m_V$ ) at maximum (Column 8) and the absolute magnitude in B band ( $M_B$ ) calculated as  $m_B - \mu_{SBF}$  (Column 9), where  $\mu_{SBF}$  is taken from Table 1. The B-band light curve fits of the SNe in the SBF sample are shown in Appendix A in Table A.2. We analyse the LCs of the SNe of the SHOES calibrator sample in the same way. The estimated LC parameters of the SHOES SNe are given in Table 3. The LC parameters of SNe in the cosmological sample are also obtained following the same fitting analysis.

### 3.2. Luminosity Calibration

Having obtained the light curve parameters, we proceed to derive the SNe Ia calibration relation separately for the SBF and the SHOES samples. Phillips (1993) gave the relation between SNe Ia luminosity and their lightcurve shape, and later Tripp (1998) added the color correction. We use this two-parameter luminosity relation including a term relating the peak luminosity of the SNe Ia to the lightcurve shape (represented by the color-stretch parameter), and a second term for the color correction accounting for the dust reddening in the host galaxy. The apparent B band peak magnitude ( $m_B$ ) of a SNe Ia is thus modelled as:

$$m_B = P^N(s_{BV} - 1) + R(m_B - m_V) + \mu_{calib} \quad (1)$$

where  $P^N$  is a polynomial of order  $N$  as a function of  $(s_{BV} - 1)$  which gives the luminosity-decline rate relation,  $R$  is the extinction correction coefficient which correlates the peak magnitude with the color ( $m_B - m_V$ ) at maximum, and  $\mu_{calib}$  is the distance modulus for the host galaxy ( $\mu_{SBF}$  taken from Table 1 for the SBF sample, and  $\mu_{ceph}$  taken from Table 5 of R16 for the SHOES sample).

Besides the Milky Way extinction correction (already included in the LC fitting procedure as described in Section 3.1), there are three other potential sources of reddening that need to be corrected for: (1) the intergalactic dust, (2) the interstellar dust of the host galaxy, and (3) the intrinsic color of SNe Ia (Burns et al. 2014; Foley & Kasen 2011; Maeda et al. 2011). To know the properties of these different sources which may vary from SN to SN, and then to disentangle their different effects requires sophisticated color modelling (see, e.g. Burns et al. 2014). Since cosmological analyses do not aim at studying the details of dust properties, we make no distinction between the intrinsic and the extrinsic sources of color variation, and combine the extinction from these different effects into the one correlation term  $R$ , as done by previous works such as Betoule et al. (2014a), Freedman et al. (2009), and Conley et al. (2011).

In order to identify the optimum model for our SBF calibrators data, we first perform the analysis using the quadratic polynomial ( $N = 2$ ) and then with only the linear polynomial ( $N = 1$ ) in  $P$ . The comparison of the luminosity-stretch ( $s_{BV}$ ) relation obtained by the two model forms shows that the second-order term does not improve the fitting. The  $R^2$  score (coefficient

of determination<sup>5</sup>) of both the fits was calculated to be 0.96 and mean squared error (MSE) as 0.06. The value of  $P^2$  parameter was estimated to be  $0.35 \pm 1.33$  which makes it consistent with zero and hence its weight in the model is null. Therefore, we use the calibration relation with the linear term in  $P^N$ :

$$m_B = P^0 + P^1(s_{BV} - 1) + R(m_B - m_V) + \mu_{calib} \quad (2)$$

### 3.3. The Hubble Constant

In order to estimate  $H_0$ , we use a purely kinematic cosmological model which gives the luminosity distance as a function of redshift (Weinberg 1972; Visser 2004). The parametrization assumes a Robertson-Walker metric in a flat space for the geometry of the universe and it is based on the Taylor series expansion of the Hubble-Lemaître law, with the presence of two additional parameters,  $q_0$  and  $j_0$ , where  $q_0 = -\ddot{a}\dot{a}^{-2}a$  is the cosmic deceleration and  $j_0 = -\ddot{a}\dot{a}^{-3}a^2$  is the third derivative of the scale factor, called cosmic jerk. For a flat universe, the expansion of the luminosity distance to the third order in  $z$  is given as:

$$d_L(z) = \frac{cz}{H_0} \left\{ 1 + \frac{1}{2}(1 - q_0)z - \frac{1}{6}(1 - q_0 - 3q_0^2 + j_0)z^2 + O(z^3) \right\} \quad (3)$$

Neglecting  $O(z^3)$  and higher order term, the corresponding distance modulus is given as:

$$\mu(z, H_0) = 5 \log_{10} \frac{cz}{H_0} \left\{ 1 + \frac{1}{2}(1 - q_0)z - \frac{1}{6}(1 - q_0 - 3q_0^2 + j_0)z^2 \right\} + 25 \quad (4)$$

For the cosmological sample, we use equation 2 except that the independent distance moduli  $\mu_{calib}$  are replaced with distance moduli as a function of  $H_0$  and the redshift as given by equation 4.  $H_0$  is left as a free parameter in the analysis. Hence the intercept term  $P^0$  is anchored only to the independent distances of the calibrator sample, and it dictates the uncertainty on the estimated Hubble constant value. We fix the value of the deceleration parameter to  $q_0 = -0.55$  and the jerk  $j_0 = 1$  (Planck Collaboration et al. 2018; Betoule et al. 2014a). In the redshift range of our SNe Ia cosmological sample ( $0.009 < z < 0.075$ ), any assumption about the expansion history of the universe does not significantly affect the final estimate of  $H_0$  (Dhawan et al. 2020). Hence, fixing the values of  $q_0$  and  $j_0$  does not bias our  $H_0$  estimates.

### 3.4. Bayesian Inference

We perform a Hierarchical Bayesian regression using the data of both the calibrator and the cosmological sample to estimate the free model parameters using Markov Chain Monte Carlo (MCMC) sampling. The Hierarchical modelling here combines two sub-models, one for the calibrator and one for the cosmological sample, and estimates the posterior distributions for the parameters of interest accounting for the similarities and preserving the uniqueness between the two samples (a partial pooling approach). Bayes' theorem gives the posterior of the model parameters as:

$$P(\Theta|D) \propto P(D|\Theta)P(\Theta) \quad (5)$$

<sup>5</sup> The  $R^2$  score is defined as  $(1 - u/v)$ , where  $u$  is the residual sum of squares  $\sum (y_{true} - y_{pred})^2$  and  $v$  is the total sum of squares  $\sum (y_{true} - \bar{y}_{true})^2$

**Table 2.** The best-fit lightcurve parameters of the SNe Ia of the SBF sample estimated using SNooPy:  $m_B$  and  $m_V$  (columns 2 and 4) are the apparent magnitudes at maximum in the B and V bands,  $s_{BV}$  (column 6) is the stretch color parameter (column 7). The color  $m_B - m_V$  (column 8) is computed as difference between the maximum magnitudes in B and V band and  $M_B$  (column 9) is the absolute magnitude in B band computed as  $m_B - \mu_{SBF}$  where  $\mu_{SBF}$  is taken from Table 1.

Supernova	$m_B$ (mag)	$\sigma_{m_B}$ (mag)	$m_V$ (mag)	$\sigma_{m_V}$ (mag)	$s_{BV}$	$\sigma_{s_{BV}}$	$m_B - m_V$ (mag)	$M_B$ (mag)
SN2000cx	13.134	0.007	13.069	0.006	0.907	0.006	0.065	-18.788
SN1994D	11.769	0.007	11.827	0.005	0.784	0.006	-0.058	-19.551
SN2007on	13.046	0.004	12.931	0.004	0.566	0.005	0.114	-18.480
SN2012cg	12.116	0.008	11.930	0.008	1.101	0.019	0.186	-18.904
SN1980N	12.459	0.011	12.334	0.012	0.848	0.011	0.125	-19.131
SN2003hv	12.455	0.049	12.544	0.036	0.764	0.020	-0.089	-19.111
SN2008Q	13.459	0.014	13.512	0.010	0.804	0.022	-0.053	-18.463
SN1970J	14.865	0.037	14.619	0.037	0.916	0.029	0.246	-18.717
SN1983G	12.789	0.102	12.614	0.071	1.189	0.059	0.175	-19.131
SN2014bv	13.999	0.018	13.809	0.013	0.640	0.021	0.190	-18.191
SN2015bp	13.697	0.014	13.664	0.016	0.681	0.018	0.033	-18.040
SN2016coj	13.205	0.021	12.978	0.013	0.891	0.011	0.227	-18.717
SN1981D	12.486	0.048	12.327	0.046	0.852	0.041	0.159	-19.104
SN1992A	12.530	0.004	12.500	0.004	0.777	0.006	0.030	-19.102
SN2018aoz	12.515	0.009	12.590	0.008	0.841	0.007	-0.075	-19.280
SN2011iv	12.446	0.008	12.389	0.009	0.652	0.014	0.057	-19.080
SN2006dd	12.270	0.003	12.287	0.003	0.950	0.003	-0.017	-19.320
SN1992bo	15.758	0.013	15.746	0.011	0.712	0.013	0.011	-18.512
SN1997E	15.171	0.009	15.082	0.007	0.795	0.012	0.090	-18.329
SN1995D	13.379	0.033	13.253	0.015	1.256	0.025	0.126	-19.221
SN1996X	13.075	0.024	13.081	0.017	0.893	0.022	-0.006	-19.185
SN1998bp	15.368	0.013	15.071	0.014	0.597	0.025	0.297	-17.732
SN2017fgc	13.619	0.019	13.345	0.014	0.957	0.018	0.273	-18.917
SN2020ue	11.970	0.011	12.071	0.008	0.718	0.012	0.101	-18.860

where  $D$  denotes the vector for the SNe observed data (the LC fit parameters  $m_B, m_V, s_{BV}$ ), and  $\Theta$  denotes the vector for the parameters of interest namely  $P^0, P^1, R$  and  $H_0$ . Then the Likelihood probability distribution  $P(D|\Theta)$  is given as the combined distribution for the calibrator and cosmological SNe:

$$P(D|\Theta) = \prod_{i=1}^{N_{calib}} P(D_i, \mu_{calib,i}|\Theta) \prod_{j=1}^{N_{cosmo}} P(D_j, z_j|\Theta, H_0) \quad (6)$$

where  $i$  is the index for the  $N_{calib}$  SNe of the calibrator sample (24 for SBF and 19 for SH0ES) and  $j$  for the  $N_{cosmo}$  SNe of the cosmological sample.  $\mu_{calib,i}$  are the independent distance estimates of the calibrating set.  $P^0, P^1, R$  and  $H_0$  are kept as free parameters and are determined simultaneously. The redshift  $z_j$  of each SN belonging to the cosmological sample is in the CMB rest frame, and is taken from the online repository as described in Section 2.3. Assuming normally distributed errors and treating the B band maximum magnitude as the target variable, the log likelihoods for the two samples can be written as:

$$\ln \mathcal{L}_{calib} = -\frac{1}{2} \sum_{i=1}^{N_{calib}} \frac{(m_B^i - m_B^T)^2}{\sigma_{calib,i}^2} - \frac{1}{2} \sum_{i=1}^{N_{calib}} \ln 2\pi \sigma_{calib,i}^2 \quad (7)$$

$$\ln \mathcal{L}_{cosmo} = -\frac{1}{2} \sum_{j=1}^{N_{cosmo}} \frac{(m_B^j - m_B^T)^2}{\sigma_{cosmo,j}^2} - \frac{1}{2} \sum_{i=j}^{N_{cosmo}} \ln 2\pi \sigma_{cosmo,j}^2 \quad (8)$$

and the combined log likelihood is:

$$\ln \mathcal{L} = \ln \mathcal{L}_{calib} + \ln \mathcal{L}_{cosmo} \quad (9)$$

Here,  $m_B^i$  is the observed B band magnitude for each supernova, and  $m_B^T$  is the true magnitude given by equation 2 for the calibrator sample and replacing  $\mu_{calib}$  with  $\mu(z, H_0)$  in that equation for the cosmological sample. The variances  $\sigma_{calib/cosmo}$  are computed as quadrature sum of the photometric errors and the SBF distance uncertainties. Additionally, in order to account for systematic uncertainties, we include two separate intrinsic scatter parameters, one each for the two samples. These two terms, namely  $\sigma_{int,calib}$  and  $\sigma_{int,cosmo}$ , are added to the variance of their respective sample and are left as free parameters in the analysis accounting for any extra dispersion observed in the measured distance moduli. So, the full variance for a given calibrator object  $i$  is

$$\sigma_{calib,i}^2 = \sigma_{m_B,i}^2 + \sigma_{\mu_{SBF},i}^2 + (P^1 \sigma_{s_{BV},i})^2 + (R \sigma_{m_B - m_V,i})^2 - 2R \sigma_{m_B,i}^2 + \sigma_{int,calib}^2 \quad (10)$$

**Table 3.** The best-fit parameters of the *SHOES* sample estimated using SNooPy.  $m_B$  and  $m_V$  (columns 2 and 4) are the apparent magnitudes at the light curve maximum in the B and V bands, respectively.  $s_{BV}$  (column 6) is the stretch color parameter (column 7). The color is given as  $m_B - m_V$  is computed as difference between the maximum magnitudes in B and V band and  $M_B$  (column 9) is the absolute magnitude in B band computed as  $m_B - \mu_{ceph}$  where  $\mu_{ceph}$  is taken from Table 5 of R16.

Supernova	$m_B$ (mag)	$\sigma_{m_B}$ (mag)	$m_V$ (mag)	$\sigma_{m_V}$ (mag)	$s_{BV}$	$\sigma_{s_{BV}}$	$m_B - m_V$ (mag)	$M_B$ (mag)
SN1995al	13.339	0.010	13.172	0.010	1.075	0.018	0.167	-19.159
SN2011by	12.889	0.009	12.821	0.009	0.947	0.007	0.068	-18.698
SN2012fr	11.976	0.006	11.943	0.004	1.122	0.009	0.033	-19.331
SN1981B	11.863	0.016	11.788	0.021	0.639	0.038	0.075	-19.043
SN2003du	13.492	0.004	13.548	0.004	1.011	0.004	-0.056	-19.427
SN2005cf	13.250	0.004	13.246	0.004	0.947	0.004	0.004	-19.013
SN2011fe	9.930	0.004	9.947	0.003	0.937	0.003	-0.017	-19.205
SN2013dy	12.757	0.004	12.554	0.003	1.136	0.010	0.203	-18.742
SN2002fk	13.205	0.023	13.209	0.017	1.189	0.034	-0.004	-19.318
SN1998aq	12.322	0.006	12.414	0.004	0.940	0.004	-0.092	-19.415
SN2007af	13.164	0.003	13.058	0.003	0.919	0.003	0.106	-18.622
SN1994ae	13.064	0.051	12.933	0.041	1.125	0.157	0.131	-19.008
SN2012cg	12.116	0.008	11.930	0.008	1.101	0.019	0.186	-18.964
SN2015F	12.823	0.009	12.695	0.010	0.865	0.007	0.128	-18.688
SN1990N	12.650	0.008	12.574	0.006	0.976	0.006	0.076	-18.882
SN2007sr	12.741	0.058	12.568	0.042	1.022	0.023	0.173	-18.549
SN2012ht	12.393	0.004	12.576	0.005	0.854	0.004	-0.183	-19.515
SN2009ig	13.478	0.008	13.372	0.007	1.134	0.023	0.106	-19.019
SN2001el	12.831	0.007	12.601	0.005	0.949	0.006	0.230	-18.480

and the total variance for an object  $j$  in cosmological sample is

$$\sigma_{cosmo,j}^2 = \sigma_{m_B,j}^2 + (P^1 \sigma_{s_{BV},j})^2 + (R \sigma_{m_B - m_V,j})^2 - 2R \sigma_{m_B,j}^2 + \sigma_{int,cosmo}^2 \quad (11)$$

Lastly, the term  $P(\Theta)$  in the equation 5 are the priors on our model parameters. We adopt uniform priors for all the parameters except the intrinsic scatter terms for which we assume a Half Cauchy distribution. The MCMC sampling is implemented using the "No U-Turn Sampler" (NUTS) provided in the PyMC3<sup>6</sup> (Salvatier et al. 2016), which is a python probabilistic programming package. Using the observed data as input, we estimate simultaneously the posteriors for the correlation parameters  $P^0, P^1, R$  and the Hubble constant  $H_0$  along with the two intrinsic scatters. All the best-fit values provided in this work are the posterior means and the errors on the parameters are the standard deviation of their posterior. The entire data sets for the three samples and the full analysis codes used in this paper are available in a GitHub repository<sup>7</sup>.

## 4. Results

### 4.1. SBF Calibration

Using the SBF calibrator sample of 24 SNe Ia and the redshift-cut cosmological sample having 96 SNe Ia ( $z > 0.02$ ), we evaluate the posterior distributions of the luminosity correlation parameters and the Hubble constant. The analysis is performed also

on the full cosmological sample of 140 SNe Ia. Table 4 gives the mean posterior values for the correlation parameters and the individual intrinsic scatters for both the SBF calibrator sample and the cosmological samples. Figure 2 shows the luminosity relations for the SBF calibration sample with respect to the stretch parameter (left panel) and the color (right panel).

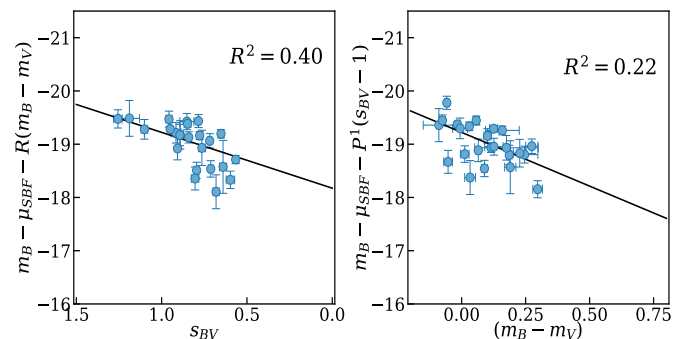


**Fig. 2.** The luminosity correlation plots for the SBF sample; the absolute magnitude ( $m_B - \mu_{SBF}$ ) corrected for the color vs the LC stretch parameter (left panel), and the absolute magnitude corrected for the LC stretch vs color (right panel). The correlation parameters are evaluated using the Bayesian analysis described in Section 3.4. The solid black lines show the best-fit model obtained with the MCMC sampling. The  $R^2$  score (coefficient of determination) of the fit is shown in the top right.

The best-fit Hubble constant value obtained using the SBF calibration on the redshift-cut cosmological sample is  $H_0 = 70.50 \pm 2.37 \text{ km s}^{-1} \text{ Mpc}^{-1}$ . It decreases to  $H_0 = 69.18 \pm 2.33 \text{ km s}^{-1} \text{ Mpc}^{-1}$  when the full cosmological sample is used. The computed  $H_0$  values are listed in the Table 5. The corner plot

<sup>6</sup> See: <https://docs.pymc.io>

<sup>7</sup> [https://github.com/nanditakhetan/SBF\\_SNeIa\\_H0](https://github.com/nanditakhetan/SBF_SNeIa_H0)

**Table 4.** Mean posterior values for the luminosity correlation parameters and associated errors for the full cosmological sample and the redshift cut sample. The last two columns in the right give the intrinsic scatters of the calibrator sample and the cosmological samples. The top part of the table shows the results obtained using the SBF calibrator sample, and the bottom part the results obtained using the *SHOES* calibrator sample.

Redshift range	$N_{sample}$	$P_0$ (mag)	$P_1$ (mag)	$R$ (mag)	$\sigma_{int,calib}$ (mag)	$\sigma_{int,cosmo}$ (mag)
<b>SBF Calibration</b>						
$0.009 < z < 0.075$	140	$-19.23 \pm 0.07$	$-1.07 \pm 0.11$	$2.03 \pm 0.16$	0.29	0.18
$0.02 < z < 0.075$	96	$-19.22 \pm 0.07$	$-1.05 \pm 0.12$	$2.01 \pm 0.17$	0.29	0.15
<b>Cepheid Calibration</b>						
$0.009 < z < 0.075$	140	$-19.16 \pm 0.05$	$-1.00 \pm 0.11$	$2.15 \pm 0.16$	0.17	0.18
$0.02 < z < 0.075$	96	$-19.16 \pm 0.05$	$-0.99 \pm 0.12$	$2.16 \pm 0.17$	0.17	0.15

showing posterior samples for SBF calibration is given in Figure B.1 of the Appendix B.

In order to investigate the influence of the adopted threshold of the  $s_{BV}$  parameter ( $s_{BV} > 0.5$ ) on our results, we evaluate the  $H_0$  removing the two transitional objects SN2007on and SN2011iv (see Section 3) from our SBF calibrator sample. The net effect is a small increase of 0.7% of the  $H_0$ . Further, assuming a more conservative definition of fast decliners in the SBF calibrator sample by removing all the SNe with  $s_{BV} < 0.7$  (5 SNe Ia including the two above transitional SNe Ia), the resultant  $H_0$  value decreases by 1.8%.

We also perform the analysis removing the object in common to the SBF and *SHOES* samples, SN2012cg, making the two calibrator samples completely independent. The  $H_0$  results from both SBF and *SHOES* calibration remain the same.

#### 4.2. Cepheid Calibration

For the Cepheid calibration, we use the *SHOES* sample as calibrator set and estimate the correlation parameters and the Hubble constant value following the same analysis as used for the SBF calibration. The estimated parameter values are listed in the lower part of the Table 4. It is worth noting the difference between the  $P_0$  values for the SBF and Cepheid calibration and the slightly higher  $R$  value for the *SHOES* calibration. The luminosity relations for the *SHOES* calibrator sample are shown in the Figure 3

Applying the *SHOES* Cepheid calibration to the redshift-cut cosmological sample, the mean value for  $H_0$  is found to be  $H_0 = 72.84 \pm 1.66 \text{ km s}^{-1} \text{ Mpc}^{-1}$ , and it decreases to  $H_0 = 71.51 \pm 1.66 \text{ km s}^{-1} \text{ Mpc}^{-1}$  when using the full cosmological sample. These values are listed in the table 5. The Hubble constant value evaluated for the redshift-cut cosmological sample is fully consistent with the measurement of R16 ( $H_0 = 73.24 \pm 1.74$ ). The posterior samples for *SHOES* calibration analysis are given in Figure B.2 of the Appendix B.

Figure 4 shows the Hubble diagram for the cosmological samples plotting the distance moduli vs the redshift. The plotted distance moduli are computed using the luminosity calibration relation obtained with the SBF sample. The solid line shows the best-fit model derived from the Bayesian regression. Residuals from the best-fit are shown in the bottom panel.

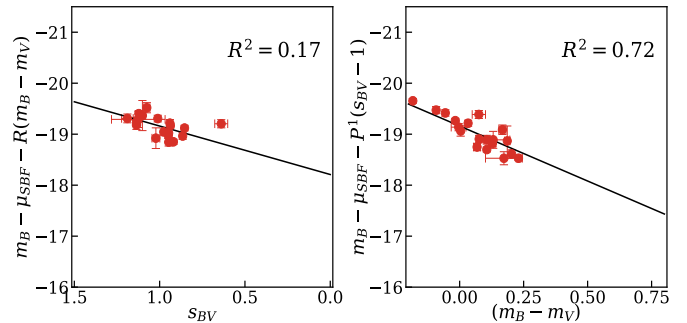


**Fig. 3.** The luminosity correlation parameters for the *SHOES* sample; the absolute magnitude ( $m_B - \mu_{SBF}$ ) corrected for the color vs the LC stretch parameter (left panel), the absolute magnitude corrected for the LC stretch vs color (right panel). The correlation parameters are evaluated using the Bayesian analysis. The solid black lines show the best-fit model obtained with the MCMC sampling. The  $R^2$  score (coefficient of determination) of the fit is shown in the top right.

#### 4.3. $H_0$ systematic uncertainties

The systematic uncertainty on  $H_0$  are calculated by combining in quadrature the systematic error on SBF measurements and those from the SNe LC fitting estimated by SNooPy. The adopted systematic errors are shown in Table 6. Our final  $H_0$  value and its uncertainties, obtained using the SBF calibration (24 SNe Ia, without including any host galaxy dependence), is  $H_0 = 70.50 \pm 2.37 (\pm 3.4\% \text{ stat}) \pm 3.38 (\pm 4.8\% \text{ sys}) \text{ km s}^{-1} \text{ Mpc}^{-1}$ .

The largest source of systematic error comes from the SBF tie to the Cepheid zero point (4.6%). The  $\sim 0.1$  mag uncertainty is derived from the scatter of the tie to Cepheids distances for the absolute SBF magnitude  $\bar{M}$  versus color relation. This scatter can be reduced with the recalibration of the Cepheid period-luminosity-metallicity (or color) relationships using Gaia parallaxes. This could halve the systematic error. Another possibility is to use the theoretical calibration of  $\bar{M}$  which makes SBF an independent primary calibrator for the distance ladder approach. The systematic error on  $H_0$  estimated using SBF SNe Ia as calibrators has a certain space for improvement.

**Table 5.**  $H_0$  values for the full cosmological sample and the redshift-cut cosmological sample which is obtained excluding the SNe Ia with  $z < 0.02$ . The  $H_0$  values are given for both the SBF (central column) and the Cepheid (right column) calibrations.

Sample cut	SBF Calibration		Cepheid Calibration	
	$H_0$	$\sigma_{H_0}$	$H_0$	$\sigma_{H_0}$
$0.009 < z < 0.075$	69.18	2.33	71.51	1.66
$0.02 < z < 0.075$	<b>70.50</b>	<b>2.37</b>	72.84	1.66

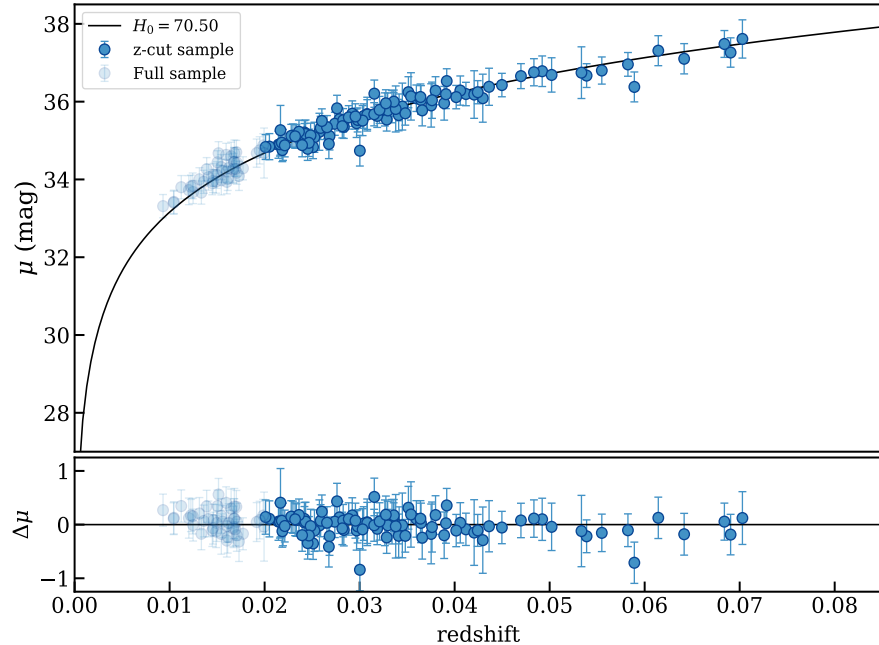


**Fig. 4.** Hubble diagram for the cosmological samples. The distance moduli of the SNe Ia are computed using the SBF calibration. The solid black line in the top panel corresponds to the  $H_0$  value estimated for the redshift-cut cosmological sample of the 96 SNe Ia with  $z > 0.02$ . The lower panel shows the residual plot.

**Table 6.** Adopted Systematic uncertainties on  $H_0$

Uncertainty	magnitude	% error
SBF tie to Cepheid ZP	0.1 mag	4.6%
B-band fit	0.012 mag	0.55 %
V-band fit	0.019 mag	0.87 %
$s_{BV}$ estimate	0.03 mag	1.4 %
Total	0.106 mag	4.8 %

## 5. Host type dependence

Considering the observational evidences that the SNe Ia luminosity correlate with the host galaxy type and its properties (Hamuy et al. 1996a; Howell 2001; Neill et al. 2009; Prughinskaya et al. 2020; Ponder et al. 2020), an additional term is typically added to the luminosity correction formula (see e.g. Betoule et al. 2014b; Rigault et al. 2015; Riess et al. 2016; Freedman et al. 2019), which takes into account the host galaxy stellar mass  $M_*$ . This stellar-mass term is considered as proxy of other galaxy properties like star-formation rate, metallicity, and/or stellar population (Sullivan et al. 2010; Kelly et al. 2010), possibly associated with different local environment and/or progenitors of the SNe Ia.

We explore also here the effect of adding the mass-based correction term (hereafter HM) to the luminosity relation of equation

2, and evaluate its influence in the  $H_0$  estimate. We adopt two recipes for the mass correction: (1) a linear correction and (2) a step correction. The luminosity relation including the HM term is:

$$m_B = P^0 + P^1(s_{BV} - 1) + R(m_B - m_V) + \text{HM} + \mu_{\text{calib}} \quad (12)$$

where the two recipes of HM can be written as,

$$\text{Step correction : HM} = \begin{cases} \alpha_{\text{step}}, & \text{for } \log_{10} M_*/M_\odot < M_{\text{step}} \\ 0, & \text{otherwise} \end{cases} \quad (13)$$

$$\text{Linear correction : HM} = \alpha_{\text{linear}}(\log_{10} M_*/M_\odot - M_0) \quad (14)$$

The step correction adds a value  $\alpha_{\text{step}}$  to the SNe absolute magnitude for all host galaxies with stellar masses below an arbitrary value  $M_{\text{step}}$  and a zero correction above it. The linear correction assumes a linear correlation of the luminosity with the host galaxy stellar mass,  $\log_{10} M_*$ , given in units of solar mass  $M_\odot$ , and  $M_0$  is again an arbitrary mass zero-point. See Appendix C for details about the estimate of the host galaxy stellar mass.

We add each of the two HM corrections to the calibration relation as in equation 12 and perform the Hierarchical Bayesian analysis described in Section 3.4 using the redshift-cut cosmological sample along with the SBF and SHOES calibrator sets one by

one. In order to see any possible effect of our arbitrary choices for the mass zero-point ( $M_0$ ) and step mass values ( $M_{step}$ ), we test it by varying these two quantities between 9 to 11.5 in steps of 0.1 and estimating  $H_0$  at each step. Plots showing this test for both the cases are given in Appendix D, Figures D.1 and D.2. We find that for the SBF calibration, both step and linear mass corrections give a  $\sim 0.7\%$  decrease in  $H_0$  compared to the  $H_0$  estimated without mass correction (noHM) for any chosen value of  $M_0$  and  $M_{step}$ . However, for the *SHOES* calibration, while the linear correction gives a  $\sim 1.3\%$  increase for any value of  $M_0$ , the step correction gives fluctuating  $H_0$  values when choosing different  $M_{step}$  values. At  $M_{step} = 9.7$ , we find a decrease of 0.7% in the  $H_0$  value with respect to the noHM calibration, which is consistent with what was found in R16 assuming  $M_{step} = 10$ . Table 7 lists the corresponding  $H_0$  values from different cases discussed here.

The mass corrections for both the SBF and *SHOES* calibrations has a small effect on the  $H_0$  estimates (ranging between 0.6% to 1.4%). The mass corrections does not resolve the difference among the  $H_0$  estimates from SBF and *SHOES* calibrations. It maintains the  $H_0$  estimate from the SBF calibration smaller than the one from the *SHOES* calibration.

## 6. SNe Ia distance comparison

In order to understand the difference in the  $H_0$  value derived using the Cepheid and the SBF calibrations, we directly focus on the comparison of the SNe Ia distance moduli obtained using the two calibrations. Using the luminosity correlation parameters inferred for SBF and *SHOES* calibrations (without the host galaxy mass correction), we evaluate the distances for the 96 SNe in the redshift-cut cosmological sample as:

$$\mu = m_B - P^0 - P^1(s_{BV} - 1) - R(m_B - m_V), \quad (15)$$

where the correlation parameter values are given in Table 4. The uncertainty  $\sigma_{\mu}^{S\text{BF}/\text{Ceph}}$  on the distance modulus of each object is computed via error propagation including the LC fitting errors and the errors on Tripp parameters computed by the Bayesian analysis. We also add in quadrature the intrinsic variance of the calibrator sample  $\sigma_{int,calib}$ . Figure 5 shows the comparison between the distance moduli of the SNe Ia obtained using the SBF (x-axis) and Cepheid (y-axis) calibration about a slope-of-unity line. The residuals ( $\mu^{\text{Ceph}} - \mu^{\text{S\text{BF}}}$ ) are plotted in the bottom panel. The distance moduli estimated with the SBF calibration result to be systematically larger than those estimated with Cepheid calibration (as shown in Fig. 5). The different  $H_0$  estimates correspond to a mean difference in distance moduli of 0.07 mag.

In order to examine the origin of this systematic difference, we inspect the SNe distances of the two calibration samples (SBF and *SHOES*). A direct comparison of distance moduli with SBF and Cepheid techniques requires that SNe Ia happened in galaxies where both SBF and Cepheid distance measurements are available. Only one object SN2012cg among our two calibrator samples satisfy this requirement for which  $\mu_{\text{S\text{BF}}} - \mu_{\text{Ceph}}$  is -0.06 mag. Since this direct comparison is not statistically significant, we compare the SNe distance moduli of the SBF and the *SHOES* samples measured by performing the same analysis as described in Section 3 but without including the cosmological sample (i.e. only  $\mathcal{L}_{calib}$  in the likelihood). Figure 6 shows the comparison of the distance moduli calibrated with the SBF and Cepheids for the two local calibration samples. For both the SBF and the *SHOES* sample SNe, the SBF calibration gives a longer distance scale than the Cepheid calibration, indicating that the difference observed in

the distance moduli of the cosmological sample comes directly from intrinsic differences in the local calibrator samples.

Ajhar et al. (2001) made a similar comparison using 14 galaxies hosting SNe Ia. They compared the SBF distances of these galaxies with the SNe Ia distances estimated using the Cepheid calibration by F01, and found them in agreement. In our SBF sample there are 9 SNe Ia in common with their paper (for 5 of them, the SBF measurement used in this paper comes directly from Ajhar et al. 2001). For these 9 objects, we find a good agreement ( $\Delta\mu \sim -0.01$  mag) between the SNe Ia distances calibrated with *SHOES* Cepheids (performing our analysis using only the local sample) and the SNe Ia distances calibrated with Cepheids by Ajhar et al. (2001) (taken from Table 3, column 5 in their paper). This comparison limited to 9/24 galaxies seems to exclude a systematic offset associated with the calibration using *SHOES* Cepheids (R16) and HST KP Cepheids (F01).

In the Appendix E (Figure E.1) we show the comparison between the directly measured SBF distances ( $\mu_{\text{S\text{BF}}}$ , given in Table 1) versus the SNe distances estimated using the SBF calibration (left plot) for the SBF sample. In the same figure we also show the plot for the *SHOES* sample, where we compare the directly measured Cepheids distances (from R16) with the distances estimated using the Cepheid calibration. In both the cases we find a good one-to-one agreement. In comparison to the Cepheids sample, the SBF sample shows a larger scatter (as indicated by  $\sigma_{int,calib}$  for SBF).

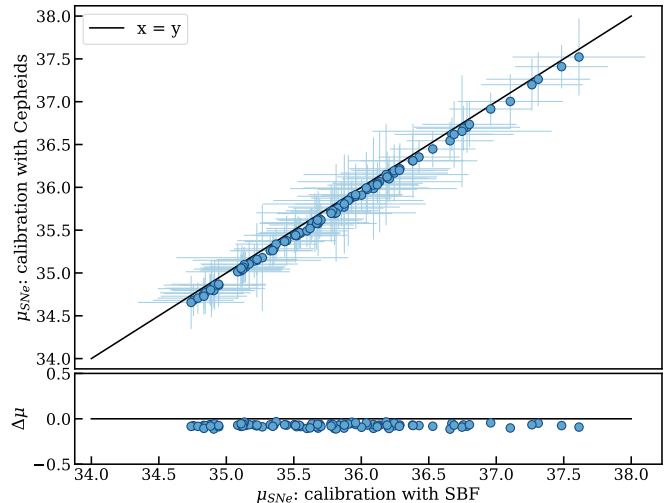


**Fig. 5.** Distance moduli of the SNe Ia belonging to the redshift-cut cosmological sample estimated using the Cepheid (y-axis) and the SBF (x-axis) as calibrator. The calibration is performed as described in Sect 3. It does not include the host galaxy mass correction. For a visual comparison, the line  $x=y$  is plotted. The bottom panel shows the residual difference among the distances calibrated by Cepheid and SBF,  $\Delta\mu = \mu^{\text{Ceph}} - \mu^{\text{S\text{BF}}}$ .

Figure 7 shows the nearby Hubble diagram for the two calibrator samples; the galaxy recessional velocity versus the distance estimated with SBF (blue data) and with the Cepheids (red data). At such distance scales, the peculiar velocities are significant with respect to the Hubble recessional velocity and need to be corrected. Here, the recessional velocity of each galaxy is corrected for peculiar velocities with the Cosmic Flow (CF) model following the analysis performed in Carrick et al. (2015). This model takes into account the influence of the large scale structures in the local Universe. The plot shows that the two samples are equally distributed and that the SBF sample reaches higher

**Table 7.** Hubble constant values estimated with applying the host mass correction to redshift-cut cosmological sample calibrated with the SBF and *SHOES* samples. The first row shows the results applying a linear mass correction, and the other rows show a mass step correction as described in the text. The last line shows the values of the  $H_0$  estimated without mass correction for comparison.

Mass Correction	SBF Calibration		Cepheid Calibration	
	$H_0$	$\sigma_{H_0}$	$H_0$	$\sigma_{H_0}$
Linear ( $M_0 = 11$ )	70.03	2.38	73.78	2.00
Step ( $M_{step} = 10$ )	70.10	2.39	72.73	1.84
Step ( $M_{step} = 9.7$ )	70.02	2.38	72.35	1.92
Step ( $M_{step} = 10.6$ )	70.14	2.42	73.83	1.84
noHM correction	70.50	2.37	72.84	1.66

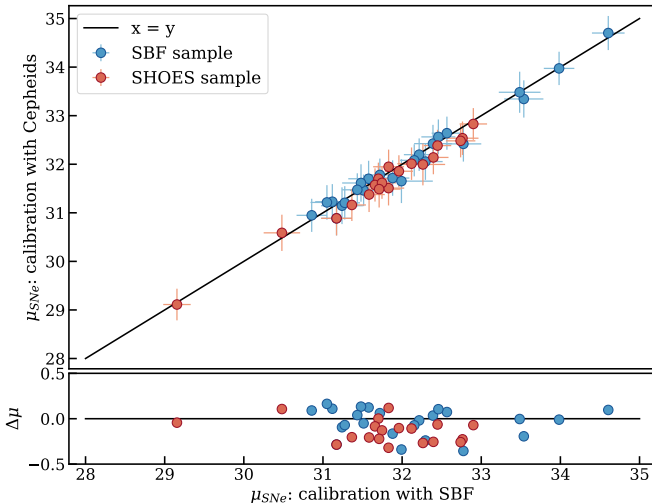


**Fig. 6.** Distance moduli of the SNe Ia belonging to the two local samples (SBF and *SHOES*) estimated using the Cepheid (y-axis) and the SBF (x-axis) as calibrator. The two calibrations used here do not include the cosmological sample in the analysis. It does not include the host galaxy mass correction. For a visual comparison, the line  $x=y$  is plotted. The bottom panel shows the residual difference among the distances calibrated by Cepheid and SBF,  $\Delta\mu = \mu^{Ceph} - \mu^{SBF}$ .

distances than the Cepheid one, enabling a larger distance range to calibrate cosmological distances.

## 7. Discussion

This work presents the first attempt to use the SBF methodology to calibrate the peak luminosity of SNe Ia. We found a mean difference of 0.07 mag between the distance moduli of the cosmological samples estimated using the SBF calibration and the ones estimated using the Cepheid calibration (corresponding difference of 3.3% between the  $H_0$  estimates from them). This difference is not accountable by an identifiable offset on the Cepheid calibration used for the SBF measurements with respect to the *SHOES* sample (see discussion on LMC distance and Cepheid  $P$ - $L$  relations in Section 2 and comparison with Ajhar et al. (2001) in Section 6).

Although, we are not able to clearly identify the cause of the difference between the SBF and Cepheid calibrated distances, our results seem to indicate that there are intrinsic differences in SNe Ia hosted in different types of environments, which are not accounted for by applying a simple host-mass correction. The different SN light curve behavior in the two samples could be

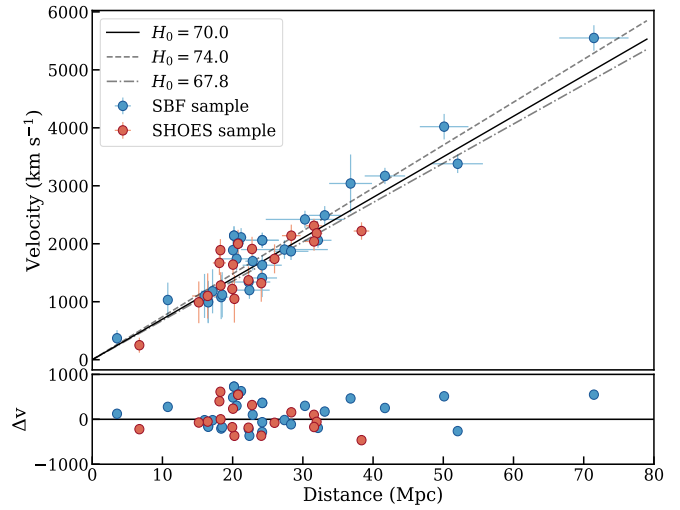


**Fig. 7.** Nearby Hubble diagram for galaxies with SBF and Cepheid distance measurements. The recessional velocities for all galaxies are corrected for peculiar motions with the CF model following Carrick et al. (2015). As a reference, also shown is the Hubble law for the values of the Hubble constant of  $H_0 = 70.0 \text{ km s}^{-1} \text{ Mpc}^{-1}$  (solid line),  $H_0 = 74.0 \text{ km s}^{-1} \text{ Mpc}^{-1}$  (dashed line) and  $H_0 = 67.8 \text{ km s}^{-1} \text{ Mpc}^{-1}$  (dot-dashed line). The bottom panel shows the residuals for both the SBF and *SHOES* samples calculated assuming a  $H_0$  of  $70 \text{ km s}^{-1} \text{ Mpc}^{-1}$ .

attributed to differences in their SNe Ia progenitors (e.g. Manucci et al. 2006; Maoz et al. 2014; Livio & Mazzali 2018), since the SBF sample is mainly composed of early E/S0 type galaxies, while the *SHOES* sample is formed of late-type spiral galaxies. Rigault et al. (2015) showed that SNe Ia in locally star-forming environments are dimmer than SNe Ia hosted in locally passive environments. In this scenario the larger distance moduli given by SBF could be due to SNe Ia exploding in older environment. Considering the general evidence that in early-type galaxies we generally observe older Population II stars while in late-type galaxies we also observe young Population I stars, difference in the evolution of the light curve in the first  $\sim 50$  days of the SN emission could be expected due to the different physical properties and composition of the SN ejecta, which can affect the amount of Fe-peak elements produced in the SN explosions. Another ingredient is how dust extinction influences the SNe Ia light curves. A comprehensive lightcurve modelling suggests that the main source of intrinsic scatter for the observed SNe Ia emission is from the extinction parameter  $R$ , which reflects variation of the dust around the SNe Ia (Brout & Scolnic 2020), although a recent detailed work on NIR SNe Ia lightcurves seems to exclude

the dust as main driver of the host galaxy and SNe Ia luminosity correlation (Ponder et al. 2020). In line with these results, we find slightly lower ( $\Delta R \sim 0.15$ ) value for the SBF sample average extinction parameter  $R$  with respect to the *SHOES* sample, see Table 5. However, this is not enough to explain the observed difference in the cosmological samples calibrated with the two methods, given that the average color ( $m_B - m_V$ ) values of the three samples in this work are way less than 1 mag. (Mean color for SBF sample: 0.09 mag, for *SHOES* sample: 0.07 mag and for cosmological sample: 0.1 mag)

### Hubble Tension

Our final  $H_0$  value estimated from SBF calibration using 24 SNe Ia applied to the redshift-cut cosmological sample is  $H_0 = 70.50 \pm 2.37$  (stat)  $\pm 3.38$  (sys)  $\text{km s}^{-1} \text{Mpc}^{-1}$ . This  $H_0$  value obtained with SBF calibration stands  $\sim 1.3\sigma$  away from both the Planck  $H_0$  estimate of the early universe (Planck Collaboration et al. 2018) and from the *SHOES* program  $H_0$  estimate (Riess et al. 2019), when we take into account only the statistical errors. Our  $H_0$  value is in good agreement with the recent estimate by Freedman et al. (2019) based on the TRGB calibration of SNe Ia. As pointed out by Freedman et al. (2020), TRGB stars populate the gas- and dust-free halos of the host galaxy in contrast to the Cepheids, which are found in the higher-surface-brightness disk regions. TRGB stars are sampling environment more similar to the SBF measurements. Figure 8 summarizes the  $H_0$  measurements in the present work for the various cases of noHM and HM corrections with SBF and *SHOES* calibrators, and shows their comparison with measurements by Planck Collaboration et al. (2018), Freedman et al. (2019), Riess et al. (2016), and Riess et al. (2019).

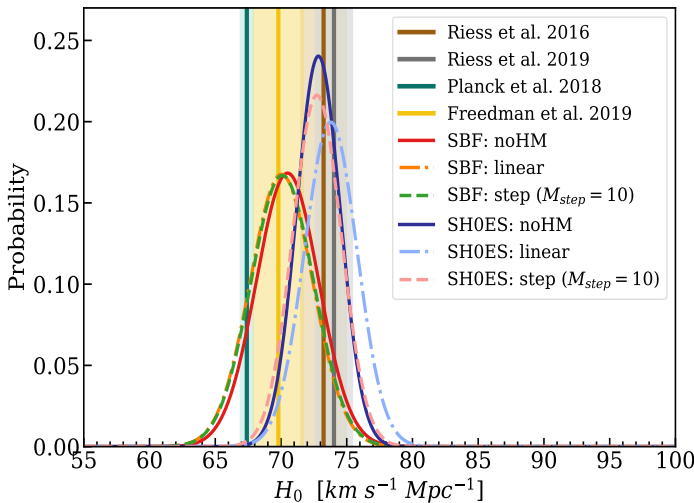


**Fig. 8.** Posterior Distributions of  $H_0$  estimated in this work with the SBF and *SHOES* calibrator samples. We give the distributions for noHM analysis (solid line), including a linear mass correction (dot-dashed line) and including a step-mass correction with  $M_{step} = 10$  (dashed line).

### Perspectives for the SNe Ia SBF calibration

The present work uses both the ground based and HST SBF optical data. In the near future, we expect major improvements in this regard by using dedicated observations by the *James Webb Space Telescope (JWST)*. The SBF method works better at the

NIR because the main source of the brightness fluctuations comes from red giant branch stars which are brighter at redder wavelengths (Blakeslee et al. 2010) and less affected by dust extinction. The red giants are excellent targets for *JWST*. However, the SBF calibration is presently not well-constrained in the NIR bands compared to the optical ones (Jensen et al. 2015). SBF offers a complementary tool to calibrate SNe Ia luminosity with respect to the Cepheids by sampling a set of different type of host galaxy environment. Although, presently SBF is a secondary distance indicator being dependent on Cepheid calibration, the theoretical calibrations which will make it an independent technique in the distance ladder (Cantiello et al. 2005) are improving.

Furthermore, SBF represents an experimental methodology which is able to anchor the distance ladder up to larger distances with respect to the Cepheid calibrations (see e.g. Fig. 7). SNe Ia being rare events, reaching larger distances will provide more galaxies hosting a SNe Ia giving us larger number of calibrators which is very important to decrease the statistical errors and reach a percent level precision goal. In this work, the measured scatter in the B-band absolute magnitudes of the fiducial calibrating sample is 0.27 mag. With 24 SBF calibrators, the uncertainty on mean absolute magnitude is 0.05 mag which corresponds to about 2.5% uncertainty in distance. While the SBF sample is expected to largely increase with the future instruments and newly discovered SNe Ia, the increase of the number of Cepheid calibrators will be limited by the smaller distance necessary for Cepheid measurements, and thus the smaller number of galaxies possibly hosting a SN explosion. The importance of having a larger number of SNe Ia calibrators is highlighted also in Freedman et al. (2019), and by Huang et al. (2020) where Mira variables have been used to calibrate SNe Ia and to measure the Hubble constant.

## 8. Conclusion and Perspectives

The primary goal of this work is to show the potential of SBF method to provide an alternative distance scale for the local universe aimed at calibrating the absolute magnitudes of SNe Ia and measuring the Hubble constant. We built a set of 24 SNe Ia calibrators having distance measurements to their hosts, mostly early-type galaxies, obtained with the SBF technique. We apply the SBF calibration to a sample of 96 SNe Ia with redshift between  $z = 0.02$  and  $z = 0.075$  (obtained from the Combined Pantheon Sample) and derived a value of  $H_0 = 70.50 \pm 2.37$  (stat)  $\pm 3.38$  (sys)  $\text{km s}^{-1} \text{Mpc}^{-1}$  (i.e.  $3.4\% \text{ stat}, 4.8\% \text{ sys}$ ), which lies in between the values obtained with SNe Ia calibrated with Cepheids and the one inferred from the analysis of the cosmic microwave background, being consistent with both of them within the errors.

We found a systematic difference of 0.07 mag among the distances estimated using the SBF calibration and the ones using the Cepheids calibration (see Figure 5). This accounts for the 3.3% smaller  $H_0$  value obtained using SBF calibration with respect the one using the *SHOES* sample as calibrator. This also explains the 5% larger  $H_0$  value of Riess et al. (2019), which uses *SHOES* sample as calibrators, compared to the SBF.

The origin of this difference is not completely understood, but it could be attributed to the different host properties of the SBF and *SHOES* calibrator samples; Cepheids are almost observed in late-type galaxies while SBF can be measured only for homogeneous passive environments like early-type and lenticular S0 galaxies. In terms of SNe Ia, different host galaxy type can translate in: a) a difference in the intrinsic dust reddening or immediate extinction, possibly due to the presence of local dense circumstellar medium; b) a different stellar population for the underlying SN progenitor, which can suggest the existence of

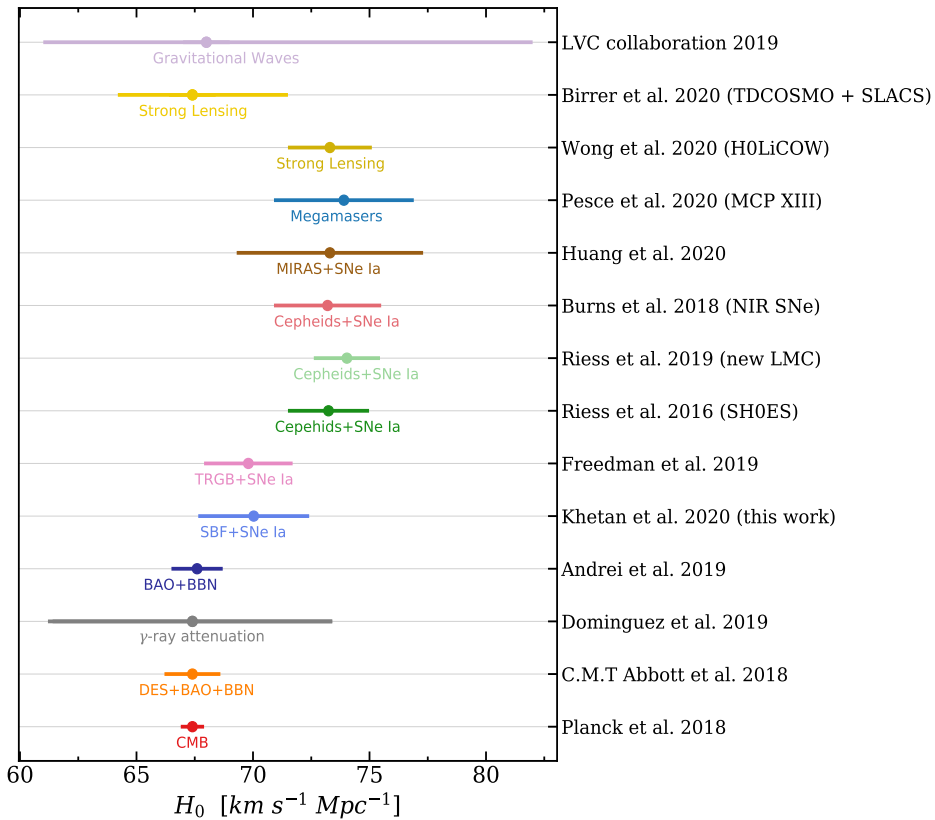


**Fig. 9.** Compilation of Hubble constant values obtained using different observations and techniques from the recent literature including the value from this work. The literature references are written on the y-axis. Two independent estimates from early universe (Planck Collaboration et al. 2016; Abbott et al. 2018) are shown at the bottom. The next is an estimate using extragalactic background light  $\gamma$  ray attenuation (Domínguez et al. 2019) and another from BAO at all redshifts + BBN estimate (Cuceu et al. 2019). Then we show measurements from SNe Ia calibrated with TRGB (Freedman et al. 2019), SNe Ia calibrated with Cepheids (SH0ES sample, Riess et al. 2016, 2019), using near-infrared (NIR) filters (Burns et al. 2018) and SNe Ia with Mira variables (Huang et al. 2020). Then we show the  $H_0$  values estimated using 6 masers in the Hubble flow (Pesce et al. 2020). The next  $H_0$  value shown is inferred via gravitational lensing time delays using six lensed quasars (Wong et al. 2020) and a more recent value obtained using 40 strong lenses (Birrer et al. 2020). Finally we shows the  $H_0$  derived with gravitational-wave signals from binary compact object mergers (The LIGO Scientific Collaboration et al. 2019).

multiple channels for the formation of the binary systems leading to a SNe Ia explosion (Mannucci et al. 2006; Foley et al. 2020); c) a difference in the metallicity or chemical composition of the underlying progenitor, which can lead to a different light curve evolution (Maoz et al. 2014; Livio & Mazzali 2018). At the moment we can neither confirm nor exclude any of the proposed possible scenarios. We believe that additional observations and analysis, in particular at NIR wavelengths where the effects of the Fe-peak elements on SNe Ia LCs are more pronounced and dust extinction is minimum, are still needed in order to shed light on this problem. Moreover, the possibility of investigating the immediate environments, using e.g. integral field spectrographs, of nearby SNe Ia can provide important clues on the fundamental physical properties of the circumstellar gas surrounding SNe Ia progenitors.

Our analysis shows that applying a correction for the host-galaxy stellar mass in the luminosity calibration relation does not reduce or correct for the possible SNe Ia luminosity dependence on galaxy types (see Section 5). This suggests the need for alternative parameter(s) which could account for the variation in the luminosity of SNe Ia hosted in different environments. This is particularly timely taking into account the upcoming observations of innovative telescopes (e.g. LSST, JWST) which are expected

to increase the number of detected SNe Ia in particular at larger redshift.

Today the value of local universe  $H_0$  is known with an uncertainty of less than 10%. However, Figure 9, which shows the current status of  $H_0$  measurements with different methodologies, reveals the existence of a dichotomy in the  $H_0$  measurements; a first group of measures characterized by a central value below  $70 \text{ km s}^{-1} \text{ Mpc}^{-1}$  and a second one centered above  $73 \text{ km s}^{-1} \text{ Mpc}^{-1}$ . The current “tension” on the  $H_0$  measurements is not only limited to CMB and Cepheids measurements but instead involves a dozen of different methods, mostly independent of each other. Our results together with the other data reported in Figure 9 suggest that there is a certain margin to interpret the discrepant results in terms of systematics while relaxing the quest for “new physics”.

**Acknowledgements.** We are grateful to Christopher Burns for his very useful comments and help with Light curve fitting using SNooPy. We thank the SN group at the Observatory of Padova, INAF for hosting NK as short-term visitor and for the valuable discussions on the nature of SNe Ia and their observation. We also extend our thanks to the researchers at the DARK Institute, Copenhagen for hosting NK as short-term visitor and discussing various details of the analysis and comments on the manuscript. NK is grateful to Jeff Cooke and CAS (Swinburne University) Melbourne for hosting her as a visiting PhD student. NK would further like to acknowledge helpful discussions with Chris Blake and Suhail Dhawan. MB, EB, and EC acknowledge financial support from MIUR (PRIN 2017 grant 20179ZF5KS). This work was supported by a VILLUM FONDEN

Investigator grant to JH (project number 16599) and by a VILLUM FONDEN Young Investigator grant to CG (project number 25501). This project is funded by the Danish council for independent research under the project ‘Fundamentals of Dark Matter Structures’, DFF - 6108-00470. Research by SV is supported by NSF grant AST-1813176.

## References

Abbott, B. P., Abbott, R., Abbott, T. D., & Acernese, F. e. a. 2017, *Nature*, 551, 85

Abbott, T. M. C., Abdalla, F. B., Annis, J., et al. 2018, *MNRAS*, 480, 3879

Ajhar, E. A., Tonry, J. L., Blakeslee, J. P., Riess, A. G., & Schmidt, B. P. 2001, *ApJ*, 559, 584

Alam, S., Ata, M., Bailey, S., et al. 2017, *MNRAS*, 470, 2617

Altavilla, G., Fiorentino, G., Marconi, M., et al. 2004, *MNRAS*, 349, 1344

Arendse, N., Wojtak, R. J., Agnello, A., et al. 2019, arXiv e-prints, arXiv:1909.07986

Aubourg, É., Bailey, S., Bautista, J. E., et al. 2015, *Phys. Rev. D*, 92, 123516

Bennett, C. L., Larson, D., Weiland, J. L., et al. 2013, *ApJS*, 208, 20

Bernal, J. L., Verde, L., & Riess, A. G. 2016, *J. Cosmology Astropart. Phys.*, 2016, 019

Betoule, M., Kessler, R., Guy, J., et al. 2014a, *A&A*, 568, A22

Betoule, M., Kessler, R., Guy, J., et al. 2014b, *A&A*, 568, A22

Birrer, S., Shajib, A. J., Galan, A., et al. 2020, arXiv e-prints, arXiv:2007.02941

Birrer, S., Treu, T., Rusu, C. E., et al. 2019, *MNRAS*, 484, 4726

Biscardi, I., Raimondo, G., Cantiello, M., & Brocato, E. 2008, *ApJ*, 678, 168

Blakeslee, J. P. 2012, *Ap&SS*, 341, 179

Blakeslee, J. P., Ajhar, E. A., & Tonry, J. L. 1999, *Astrophysics and Space Science Library*, Vol. 237, *Distances from Surface Brightness Fluctuations*, ed. A. Heck & F. Caputo, 181

Blakeslee, J. P., Cantiello, M., Mei, S., et al. 2010, *ApJ*, 724, 657

Blakeslee, J. P., Jordán, A., Mei, S., et al. 2009a, *ApJ*, 694, 556

Blakeslee, J. P., Jordán, A., Mei, S., et al. 2009b, *ApJ*, 694, 556

Blakeslee, J. P., Lucey, J. R., Tonry, J. L., et al. 2002, *MNRAS*, 330, 443

Blakeslee, J. P., Vazdekis, A., & Ajhar, E. A. 2001, *MNRAS*, 320, 193

Brocato, E., Capaccioli, M., & Condelli, M. 1998, *Mem. Soc. Astron. Italiana*, 69, 155

Brout, D. & Scolnic, D. 2020, arXiv e-prints, arXiv:2004.10206

Brown, P. J., Breeveld, A. A., Holland, S., Kuin, P., & Pritchard, T. 2014, *Ap&SS*, 354, 89

Burns, C. R., Parent, E., Phillips, M. M., et al. 2018, *ApJ*, 869, 56

Burns, C. R., Stritzinger, M., Phillips, M. M., et al. 2014, *ApJ*, 789, 32

Burns, C. R., Stritzinger, M., Phillips, M. M., et al. 2011, *AJ*, 141, 19

Cadonau, R. & Leibundgut, B. 1990, *A&AS*, 82, 145

Cantiello, M., Blakeslee, J., Raimondo, G., Brocato, E., & Capaccioli, M. 2007, *The Astrophysical Journal*, 668, 130

Cantiello, M., Blakeslee, J. P., Ferrarese, L., et al. 2018a, *ApJ*, 856, 126

Cantiello, M., Blakeslee, J. P., Raimondo, G., et al. 2005, *ApJ*, 634, 239

Cantiello, M., Grado, A., Blakeslee, J. P., et al. 2013, *A&A*, 552, A106

Cantiello, M., Jensen, J. B., Blakeslee, J. P., et al. 2018b, *ApJ*, 854, L31

Cantiello, M., Raimondo, G., Brocato, E., & Capaccioli, M. 2003, *AJ*, 125, 2783

Carrick, J., Turnbull, S. J., Lavaux, G., & Hudson, M. J. 2015, *MNRAS*, 450, 317

Cole, S., Percival, W. J., Peacock, J. A., et al. 2005, *MNRAS*, 362, 505

Conley, A., Guy, J., Sullivan, M., et al. 2011, *ApJS*, 192, 1

Contreras, C., Hamuy, M., Phillips, M. M., et al. 2010, *AJ*, 139, 519

Cuceu, A., Farr, J., Lemos, P., & Font-Ribera, A. 2019, *J. Cosmology Astropart. Phys.*, 2019, 044

Dhawan, S., Brout, D., Scolnic, D., et al. 2020, *ApJ*, 894, 54

Dhawan, S., Jha, S. W., & Leibundgut, B. 2018, *A&A*, 609, A72

Domínguez, A., Wojtak, R., Finke, J., et al. 2019, *ApJ*, 885, 137

Eisenstein, D. J., Zehavi, I., Hogg, D. W., et al. 2005, *ApJ*, 633, 560

Ferrarese, L., Mould, J. R., Kennicutt, Robert C., J., et al. 2000, *ApJ*, 529, 745

Folatelli, G., Phillips, M. M., Burns, C. R., et al. 2010, *AJ*, 139, 120

Foley, R. J., Hoffmann, S. L., Macri, L. M., et al. 2020, *MNRAS*, 491, 5991

Foley, R. J. & Kasen, D. 2011, *ApJ*, 729, 55

Freedman, W. L., Burns, C. R., Phillips, M. M., et al. 2009, *ApJ*, 704, 1036

Freedman, W. L. & Madore, B. F. 2010, *ARA&A*, 48, 673

Freedman, W. L., Madore, B. F., Gibson, B. K., et al. 2001, *ApJ*, 553, 47

Freedman, W. L., Madore, B. F., Hatt, D., et al. 2019, *ApJ*, 882, 34

Freedman, W. L., Madore, B. F., Hoyt, T., et al. 2020, *ApJ*, 891, 57

Freedman, W. L., Madore, B. F., Scowcroft, V., et al. 2012, *ApJ*, 758, 24

Gaia Collaboration, Brown, A. G. A., Vallenari, A., et al. 2018, *A&A*, 616, A1

Gall, C., Stritzinger, M. D., Ashall, C., et al. 2018, *A&A*, 611, A58

Guillochon, J., Parrent, J., Kelley, L. Z., & Margutti, R. 2017, *ApJ*, 835, 64

Gupta, R. R., D’Andrea, C. B., Sako, M., et al. 2011, *ApJ*, 740, 92

Hamuy, M., Phillips, M. M., Maza, J., et al. 1991, *AJ*, 102, 208

Hamuy, M., Phillips, M. M., Suntzeff, N. B., et al. 1996a, *AJ*, 112, 2408

Hamuy, M., Phillips, M. M., Suntzeff, N. B., et al. 1996b, *AJ*, 112, 2408

Hayden, B. T., Gupta, R. R., Garnavich, P. M., et al. 2013, *ApJ*, 764, 191

Hicken, M., Challis, P., Jha, S., et al. 2009a, *ApJ*, 700, 331

Hicken, M., Challis, P., Kirshner, R. P., et al. 2012, *ApJS*, 200, 12

Hicken, M., Wood-Vasey, W. M., Blondin, S., et al. 2009b, *ApJ*, 700, 1097

Hoffmann, S. L., Macri, L. M., Riess, A. G., et al. 2016, *ApJ*, 830, 10

Howell, D. A. 2001, *ApJ*, 554, L193

Hsiao, E. Y., Conley, A., Howell, D. A., et al. 2007, *ApJ*, 663, 1187

Huang, C. D., Riess, A. G., Yuan, W., et al. 2020, *ApJ*, 889, 5

Jensen, J. B., Blakeslee, J. P., Gibson, Z., et al. 2015, *ApJ*, 808, 91

Jensen, J. B., Tonry, J. L., Barris, B. J., et al. 2003, *ApJ*, 583, 712

Jensen, J. B., Tonry, J. L., Thompson, R. I., et al. 2001, *ApJ*, 550, 503

Jha, S., Kirshner, R. P., Challis, P., et al. 2006, *AJ*, 131, 527

Kang, Y., Lee, Y.-W., Kim, Y.-L., Chung, C., & Ree, C. H. 2019, arXiv e-prints, arXiv:1912.04903

Kelly, P. L., Hicken, M., Burke, D. L., Mandel, K. S., & Kirshner, R. P. 2010, *ApJ*, 715, 743

Kennicutt, Robert C., J., Stetson, P. B., Saha, A., et al. 1998, *ApJ*, 498, 181

Lampeitl, H., Smith, M., Nichol, R. C., et al. 2010, *ApJ*, 722, 566

Li, W., Filippenko, A. V., Gates, E., et al. 2001, *PASP*, 113, 1178

Livio, M., & Mazzali, P. 2018, *Phys. Rep.*, 736, 1

Macaulay, E., Nichol, R. C., Bacon, D., et al. 2019, *MNRAS*, 486, 2184

Madore, B. F. & Freedman, W. L. 1991, *PASP*, 103, 933

Maeda, K., Leloudas, G., Taubenberger, S., et al. 2011, *MNRAS*, 413, 3075

Mannucci, F., Della Valle, M., & Panagia, N. 2006, *MNRAS*, 370, 773

Maoz, D., Mannucci, F., & Nelemans, G. 2014, *ARA&A*, 52, 107

Marin-Franch, A., & Aparicio, A. 2006, *A&A*, 450, 979

Mei, S., Blakeslee, J. P., Tonry, J. L., et al. 2005, *ApJ*, 625, 121

Mei, S., Scoggio, M., Silva, D. R., & Quinn, P. J. 2003, *A&A*, 399, 441

Mörtsell, E. & Dhawan, S. 2018, *J. Cosmology Astropart. Phys.*, 2018, 025

Neill, J. D., Sullivan, M., Howell, D. A., et al. 2009, *ApJ*, 707, 1449

Perlmutter, S., Gabi, S., Goldhaber, G., et al. 1997, *ApJ*, 483, 565

Pesce, D. W., Braatz, J. A., Reid, M. J., et al. 2020, *ApJ*, 891, L1

Phillips, M. M. 1993, *ApJ*, 413, L105

Phillips, M. M., Contreras, C., Hsiao, E. Y., et al. 2019, *PASP*, 131, 014001

Pietrzynski, G., Graczyk, D., Galle, A., et al. 2019, *Nature*, 567, 200

Pietrzynski, G., Graczyk, D., Gieren, W., et al. 2013, *Nature*, 495, 76

Planck Collaboration, Ade, P. A. R., Aghanim, N., et al. 2016, *A&A*, 594, A13

Planck Collaboration, Aghanim, N., Akrami, Y., et al. 2018, arXiv e-prints, arXiv:1807.06209

Ponder, K. A., Wood-Vasey, W. M., Weyant, A., et al. 2020, arXiv e-prints, arXiv:2006.13803

Pruzhinskaya, M., Novinskaya, A., Pauna, N., & Rosnet, P. 2020, arXiv e-prints, arXiv:2006.09433

Raimondo, G., Brocato, E., Cantiello, M., & Capaccioli, M. 2005, *AJ*, 130, 2625

Richmond, M. & Vietje, B. 2017, *Journal of the American Association of Variable Star Observers (AAVSO)*, 45, 65

Richmond, M. W., Treffers, R. R., Filippenko, A. V., et al. 1995, *AJ*, 109, 2121

Riess, A. G., Casertano, S., Yuan, W., Macri, L. M., & Scolnic, D. 2019, *ApJ*, 876, 85

Riess, A. G., Kirshner, R. P., Schmidt, B. P., et al. 1999, *AJ*, 117, 707

Riess, A. G., Li, W., Stetson, P. B., et al. 2005, *ApJ*, 627, 579

Riess, A. G., Macri, L., Casertano, S., et al. 2011, *ApJ*, 730, 119

Riess, A. G., Macri, L. M., Hoffmann, S. L., et al. 2016, *ApJ*, 826, 56

Riess, A. G., Press, W. H., & Kirshner, R. P. 1996, *ApJ*, 473, 88

Rigault, M., Aldering, G., Kowalski, M., et al. 2015, *ApJ*, 802, 20

Rigault, M., Copin, Y., Aldering, G., et al. 2013, *A&A*, 560, A66

Roman, M., Hardin, D., Betoule, M., et al. 2018, *A&A*, 615, A68

Salvatier, J., Wiecki, T. V., & Fonnesbeck, C. 2016, *PeerJ Computer Science*, 2, e55

Sandage, A., Tammann, G. A., Saha, A., et al. 2006, *ApJ*, 653, 843

Schlafly, E. F. & Finkbeiner, D. P. 2011, *ApJ*, 737, 103

Scolnic, D., Casertano, S., Riess, A., et al. 2015, *ApJ*, 815, 117

Scolnic, D. M., Jones, D. O., Rest, A., et al. 2018, *ApJ*, 859, 101

Silverman, J. M., Foley, R. J., Filippenko, A. V., et al. 2012, *MNRAS*, 425, 1789

Skrutskie, M. F., Cutri, R. M., Stiening, R., et al. 2006a, *AJ*, 131, 1163

Skrutskie, M. F., Cutri, R. M., Stiening, R., et al. 2006b, *AJ*, 131, 1163

Sorce, J. G., Courtois, H. M., Tully, R. B., et al. 2013, *ApJ*, 765, 94

Stritzinger, M., Burns, C. R., Phillips, M. M., et al. 2010, *AJ*, 140, 2036

Stritzinger, M. D., Phillips, M. M., Boldt, L. N., et al. 2011, *AJ*, 142, 156

Sullivan, M., Conley, A., Howell, D. A., et al. 2010, *MNRAS*, 406, 782

Suyu, S. H., Bonvin, V., Courbin, F., et al. 2017, *MNRAS*, 468, 2590

The LIGO Scientific Collaboration, the Virgo Collaboration, Abbott, B. P., et al. 2019, arXiv e-prints, arXiv:1908.06060

Tody, D. 1986, *Society of Photo-Optical Instrumentation Engineers (SPIE) Conference Series*, Vol. 627, *The IRAF Data Reduction and Analysis System*, ed. D. L. Crawford, 733

Tonry, J. & Schneider, D. P. 1988, *AJ*, 96, 807

Tonry, J. L., Dressler, A., Blakeslee, J. P., et al. 2001, *ApJ*, 546, 681

Tripp, R. 1998, *A&A*, 331, 815

Tsvetkov, D. Y. 1982, *Soviet Astronomy Letters*, 8, 115

Udalski, A., Szymanski, M., Kubiak, M., et al. 1999, *Acta Astron.*, 49, 201

Verde, L., Treu, T., & Riess, A. G. 2019, *Nature Astronomy*, 3, 891

Vinkó, J., Ordasi, A., Szalai, T., et al. 2018, *PASP*, 130, 064101

Visser, M. 2004, *Classical and Quantum Gravity*, 21, 2603

Weinberg, S. 1972, *Gravitation and Cosmology: Principles and Applications of the General Theory of Relativity*

Wen, X.-Q., Wu, H., Zhu, Y.-N., et al. 2013, *MNRAS*, 433, 2946

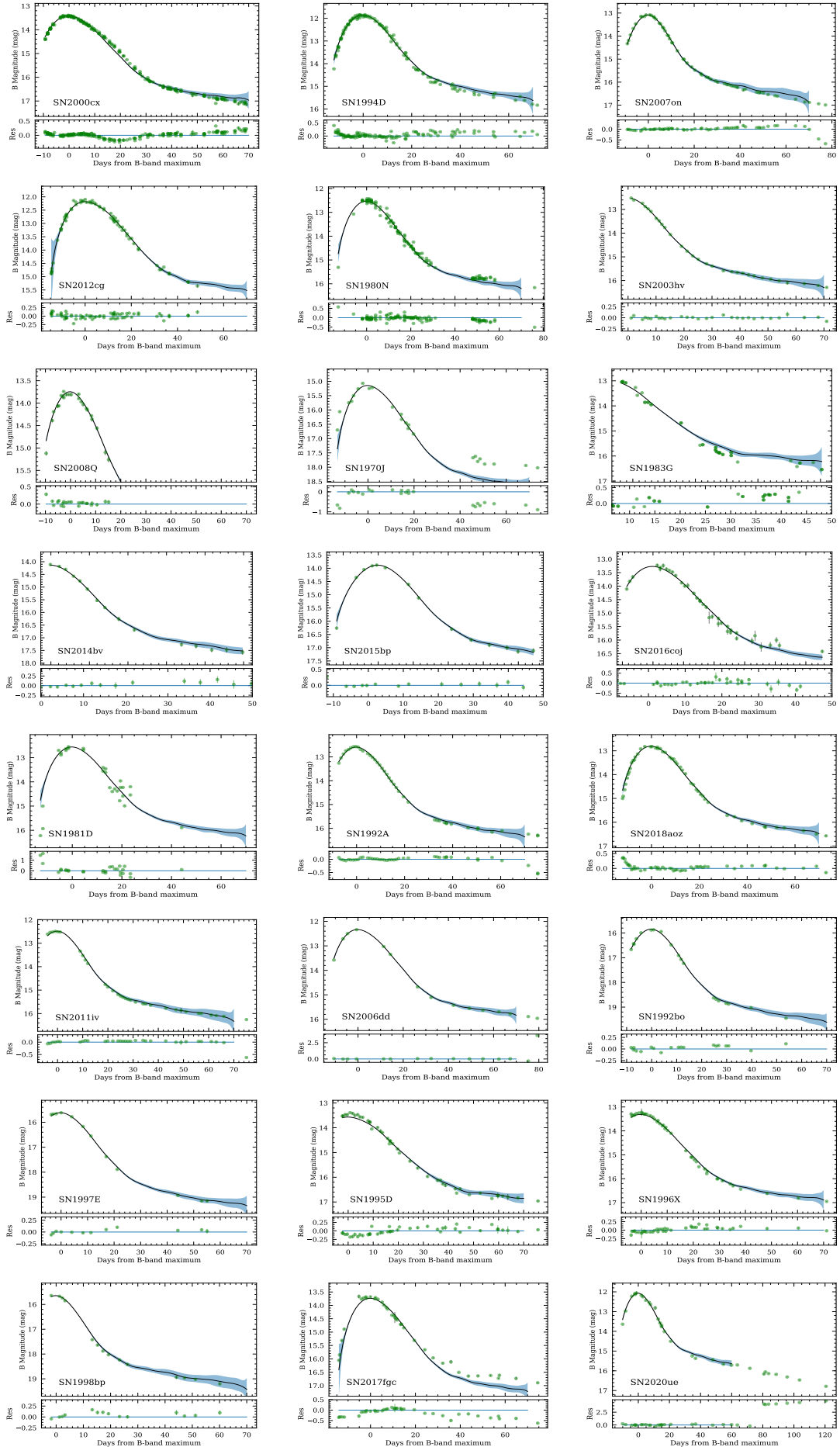
Wong, K. C., Suyu, S. H., Chen, G. C. F., et al. 2020, *MNRAS*[arXiv: 1907.04869]

Yuan, W., Riess, A. G., Macri, L. M., Casertano, S., & Scolnic, D. M. 2019, *ApJ*, 886, 61

## Appendix A: Light Curve Fitting with SNooPy

**Table A.1.** Literature references for the optical photometry data of the SNe Ia in the SBF calibrator sample.

Supernova	Host Galaxy	Photometry Reference
SN2000cx	NGC524	<a href="#">Li et al. (2001)</a>
SN1994D	NGC4526	<a href="#">Richmond et al. (1995)</a>
SN2007on	NGC1404	<a href="#">Stritzinger et al. (2011)</a>
SN2012cg	NGC4424	<a href="#">Vinkó et al. (2018)</a>
SN1981B	NGC4536	<a href="#">Tsvetkov (1982)</a>
SN2003hv	NGC1201	<a href="#">Silverman et al. (2012)</a>
SN2008Q	NGC524	<a href="#">Brown et al. (2014)</a>
SN1970J	NGC7619	<a href="#">Cadonau &amp; Leibundgut (1990)</a>
SN1983G	NGC4753	<a href="#">Cadonau &amp; Leibundgut (1990)</a>
SN2014bv	NGC4386	<a href="#">Brown et al. (2014)</a>
SN2015bp	NGC5839	<a href="#">Brown et al. (2014)</a>
SN2016coj	NGC4125	<a href="#">Richmond &amp; Vietje (2017)</a>
SN1981D	NGC1316	<a href="#">Hamuy et al. (1991)</a>
SN1992A	NGC1380	<a href="#">Altavilla et al. (2004)</a>
SN2018aoz	NGC3923	<a href="#">Ni et al. <i>in prep</i></a>
SN2011iv	NGC1404	<a href="#">Gall et al. (2018)</a>
SN2006dd	NGC1316	<a href="#">Stritzinger et al. (2010)</a>
SN1992bo	E352-057	<a href="#">Hamuy et al. (1996b)</a>
SN1997E	NGC2258	<a href="#">Jha et al. (2006)</a>
SN1995D	NGC2962	<a href="#">Riess et al. (1999)</a>
SN1996X	NGC5061	<a href="#">Riess et al. (1999)</a>
SN1998bp	NGC6495	<a href="#">Jha et al. (2006)</a>
SN2017fgc	NGC0474	<a href="#">Burke et al. <i>in prep</i></a>
SN2020ue	NGC4636	<a href="#">Khetan et al. <i>in prep</i></a>

**Table A.2.** The table of figures gives the B-band LC fits of the 24 SNe Ia in the SBF calibrator sample. The fits are done using SNooPy.

## Appendix B: corner plots

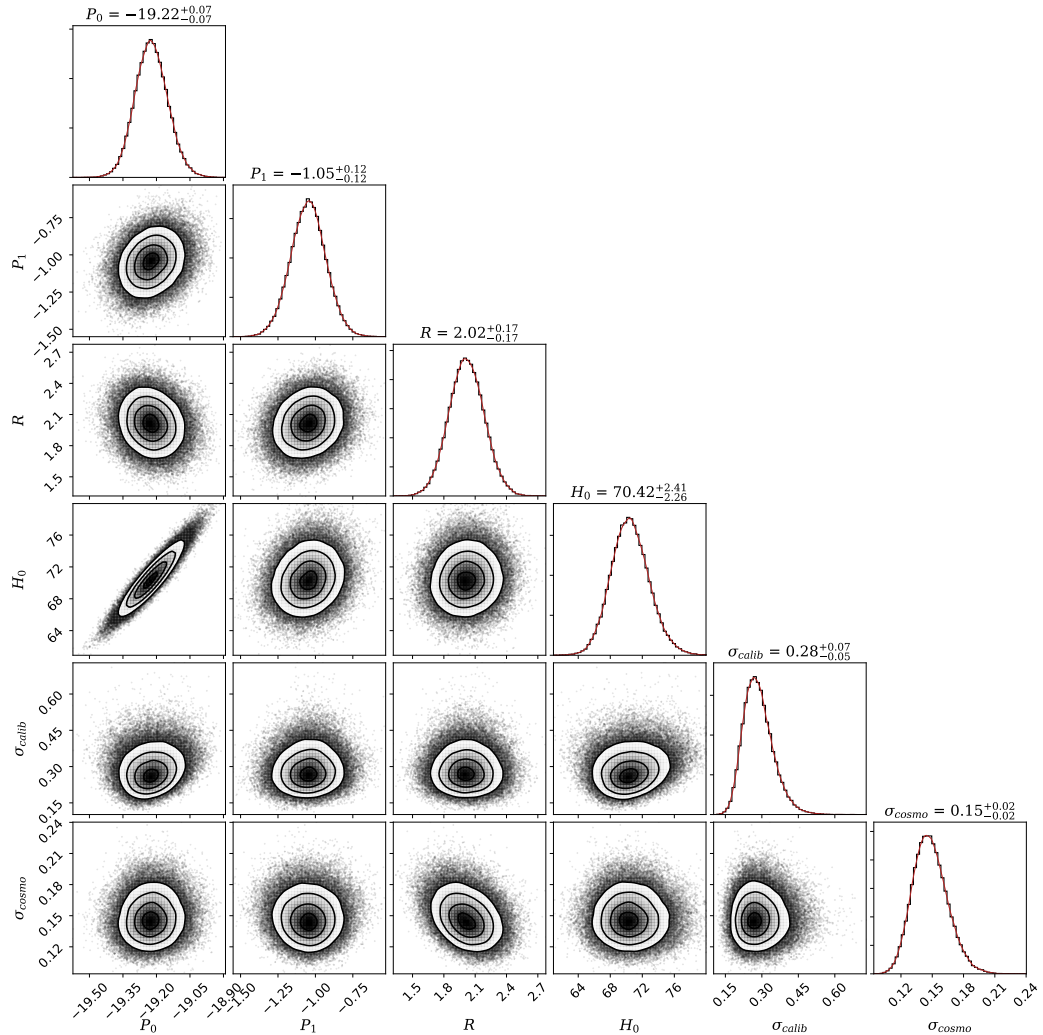


**Fig. B.1.** Corner plot showing posterior distributions for the parameters  $P_0$ ,  $P_1$ ,  $R$  and  $H_0$  along with the intrinsic scatters obtained using the SBF sample (24 SNe Ia) with the redshift cut cosmological sample (96 SNe Ia). The title on each histogram shows the median value of the respective posterior distribution. The luminosity correction does not include any dependence in host galaxy stellar mass.

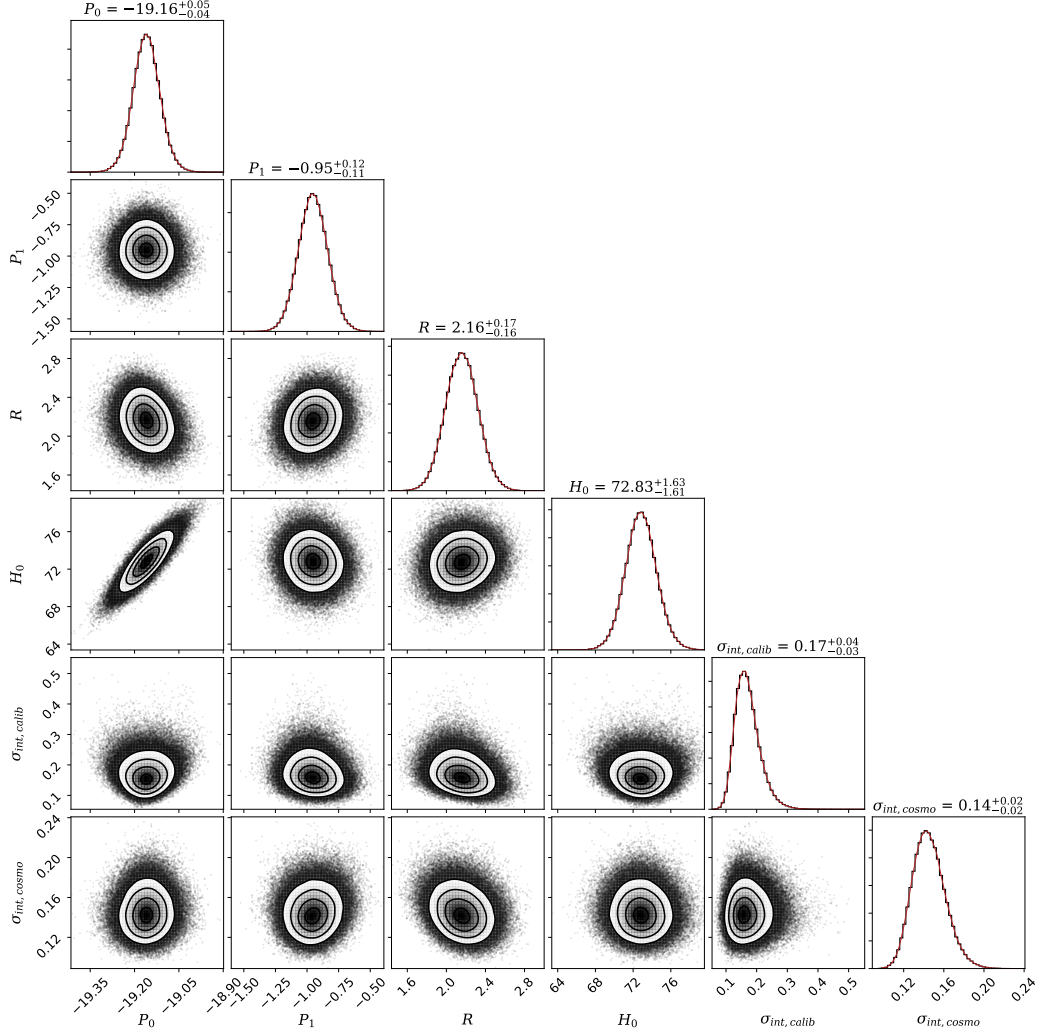


**Fig. B.2.** Corner plot showing posterior distributions for the parameters  $P_0$ ,  $P_1$ ,  $R$  and  $H_0$  along with the intrinsic scatters obtained using the *SHOES* sample with the redshift cut cosmological sample. The title on each histogram shows the median value of the respective posterior distribution. The luminosity correction does not include any dependence in host galaxy stellar mass.

## Appendix C: Host galaxy stellar-mass evaluation

The stellar mass of the host galaxies of the two calibrator samples, SBF and *SH0ES* and the cosmological sample are evaluated using the approach described in the following. The mass for each galaxy is determined using the 2MASS extended source catalog (Skrutskie et al. 2006b). We use the  $K_s$ -band magnitude for each galaxy and correct it for the extinction. Then, assuming a constant mass-to-light ratio, the stellar mass of the host galaxy is evaluated using an empirical relation derived by Wen et al. (2013):

$$\log_{10}\left(\frac{M_*}{M_\odot}\right) = (-0.498 \pm 0.002) + (1.105 \pm 0.001) \times \log_{10}\left(\frac{\nu L_\nu(K_s)}{L_\odot}\right) \quad (\text{C.1})$$

Where  $L_\nu(K_s)$  is the  $K_s$ -band luminosity and 1.105 is the mass-to-light ratio. However, the calculation of  $L_\nu(K_s)$  requires to know the distance modulus of the galaxy and hence it introduces a covariance in host mass with the estimated distances (Hubble residual) and should be dealt carefully. Solving the above equation by translating  $L_\nu(K_s)$  into  $\mu$ , one finds that  $\log_{10}(M_*/M_\odot) \propto 0.4\mu$ , and therefore we include  $0.4\delta\mu^2$  error in our calibration calculations where  $\delta\mu$  is the error on the distance modulus. To estimate the error on the stellar mass, we use the standard error propagation. For the *SH0ES* calibrator sample, two galaxies, NGC4038 and UGC9391 (corresponding to SN2007sr and SN2003du, respectively) are not in the 2MASS catalog. For their mass calculation we evaluate the magnitude directly from the  $K_s$ -band images. We first flag the foreground stars and replace with random neighbouring background pixels using imedit in IRAF (Tody 1986), and then we subtract the sky background. The total flux within an ellipse of appropriate size is measured, which is then converted to stellar mass using the same method and mass-to-light ratio as described above.

## Appendix D: Step and Linear Mass correction

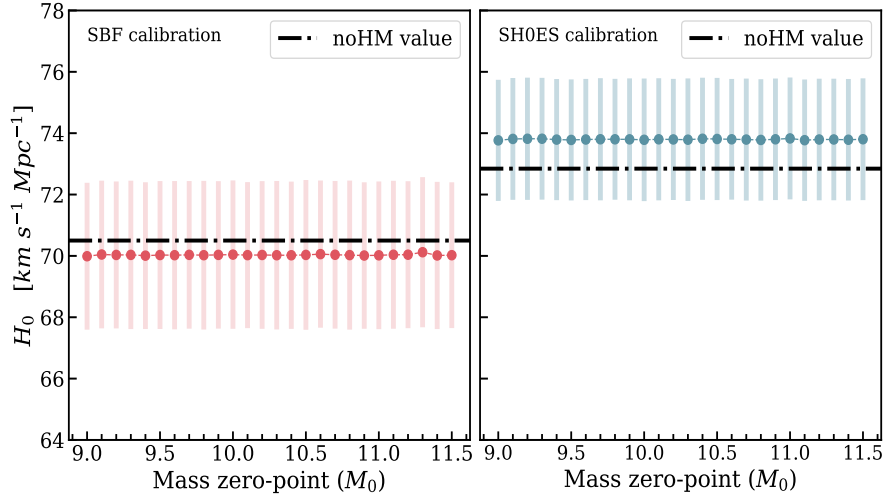


**Fig. D.1.**  $H_0$  values estimated including the linear mass correction in the calibration at different values of  $M_0$ . For the SBF calibration (left panel), the linear mass correction decreases the value of  $H_0$  by  $\sim 0.6\%$  with respect to the  $H_0$  estimated without mass correction (noHM value, shown in dotted black line) for any chosen value of  $M_0$ . For the SH0ES calibration (right panel), we see an increase of  $1.3\%$  from the noHM value. This justifies an arbitrary choice for  $M_0$ .

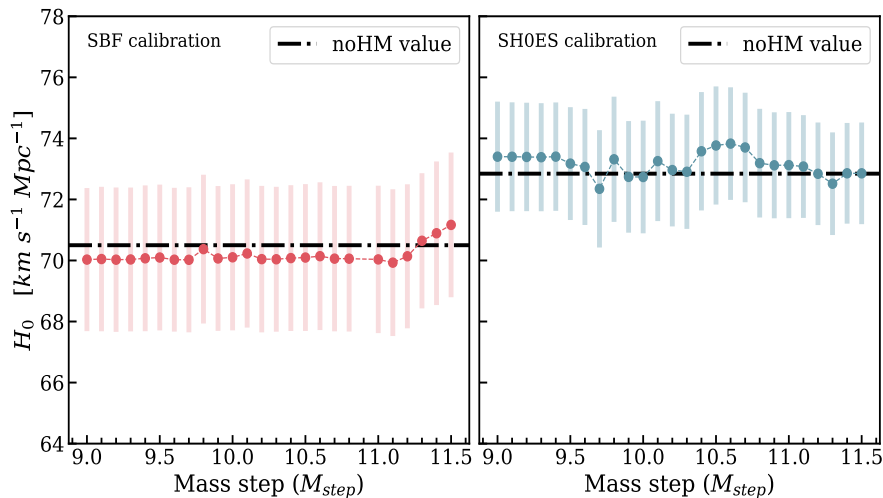


**Fig. D.2.**  $H_0$  values estimated including the Step mass correction in the calibration at different values of  $M_{step}$ . The SBF calibration with a step mass correction deceases the  $H_0$  value by  $\sim 0.5\%$  almost consistently at each  $M_{step}$  except at the extreme end. However, for the SH0ES calibration, step based correction gives fluctuating values. The lowest value is found at  $M_{step} = 9.7$  and is  $0.7\%$  lower than the noHM value and the highest is found for  $M_{step} = 10.6$  which is  $1.4\%$  higher than the noHM value of  $H_0$ .

## Appendix E: Local sample comparison

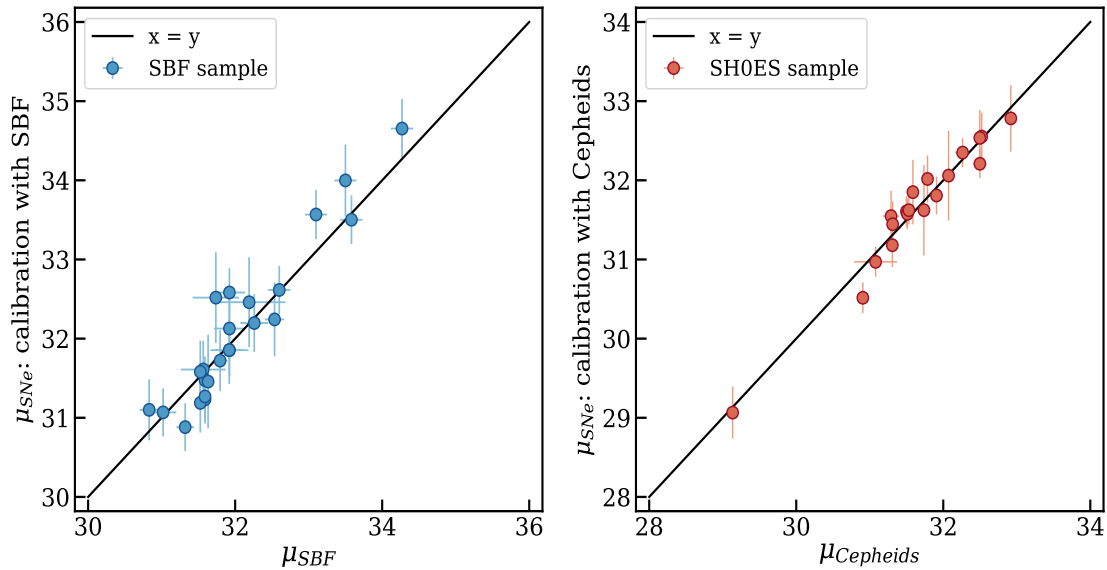


**Fig. E.1.** Distance moduli comparisons of the two local calibrator samples. The left plot shows the comparison between directly measured SBF distances ( $\mu_{SBF}$ , given in Table 1) for the SBF sample with the SNe distances estimated using the SBF calibration of the cosmological redshift-cut sample of 96 SNe as described in Section 3. The right plot shows similar comparison for the *SH0ES* sample, comparing the measured cepheid distances (from R16) with the distances estimated using the Cepheid calibration of the cosmological redshift-cut sample. In both the cases we find a good one-to-one agreement.